Internal dynamics of Abell 2254: a merging galaxy cluster with a clumpy, diffuse radio emission

M. Girardi[1,2], S. Bardelli[3], R. Barrena[4,5], W. Boschin[6], F. Gastaldello[7,8], and M. Nonino[2]

[1] Dipartimento di Fisica dell'Università degli Studi di Trieste - Sezione di Astronomia, via Tiepolo 11, I-34143 Trieste, Italy

[2] INAF - Osservatorio Astronomico di Trieste, via Tiepolo 11, I-34143 Trieste, Italy

[3] INAF - Osservatorio Astronomico di Bologna, via Ranzani 1, I-40127, Bologna, Italy

[4] Instituto de Astrofísica de Canarias, C/Vía Láctea s/n, E-38205 La Laguna (Tenerife), Canary Islands, Spain

[5] Departamento de Astrofísica, Universidad de La Laguna, Av. del Astrofísico Franciso Sánchez s/n, E-38205 La Laguna (Tenerife), Canary Islands, Spain

[6] Fundación Galileo Galilei - INAF, Rambla José Ana Fernández Perez 7, E-38712 Breña Baja (La Palma), Canary Islands, Spain

[7] INAF-IASF Milano, Via Bassini 15, I-20133 Milano, Italy

[8] Department of Physics and Astronomy, University of California at Irvine, 4129, Frederick Reines Hall, Irvine, CA, 92697-4575, USA

ABSTRACT

Context. The mechanisms giving rise to diffuse radio emission in galaxy clusters, and in particular their connection with cluster mergers, are still debated.

Aims. We explore the internal dynamics of Abell 2254, which has been shown to host a very clumpy and irregular radio halo.

Methods. Our analysis is mainly based on redshift data for 128 galaxies acquired at the Telescopio Nazionale Galileo. We combine galaxy velocities and positions to select 110 cluster galaxies and analyze its internal dynamics. We also use new (g', r', i') photometric data acquired at the Isaac Newton Telescope and (V,i') photometric data available in the Subaru Archive. X-ray data from the XMM-Newton Science Archive are analyzed to study the hot gas component.

Results. We estimate the cluster redshift $\langle z \rangle = 0.177$, a high line-of-sight (LOS) velocity dispersion, $\sigma_V \sim 1350$ km s^{-1} , and the X-ray temperature $kT \sim 6.4$ keV. Both our optical and X-ray analyses reveal a complex dynamical activity. The analysis of the 2D galaxy distribution reveals the presence of two density peaks, one at the East and the other at the West. Using the full 3D information we detect a high velocity ($\Delta V_{\rm rf,LOS} \sim 3000$ km s^{-1}), low mass ($\sigma_V \sim 200$–500 km s^{-1}) group at the position of the 2D eastern peak. For the main system we compute a velocity dispersion $\sigma_V \sim 1000$–1200 km s^{-1}. In the assumption of a bimodal system we estimate a mass $M_{\rm sys} = 1.5$–2.9×10^{15} h_{70}^{-1} $M_\odot$. The X-ray morphological analysis, based on power ratios, centroid shifts, and concentration parameter, confirms that Abell 2254 is a dynamically disturbed cluster. The X-ray isophotes are elongated toward the eastern direction, in agreement with a merger in the post core-crossing phase. A simple bimodal model finds that data are consistent with a bound, outgoing subcluster observed a few fractions of Gyr after the core crossing. However, both optical and X-ray analyses suggest that the main system is, at its time, a non relaxed structure, indicating N-S as a possible direction for a past accretion.

Conclusions. We conclude that Abell 2254, for its mass and merging structure, fits well among typical clusters with radio halos. We shortly discuss as the particular irregularity of the radio halo might be linked to the complexity of the Abell 2254 structure.

Key words. Galaxies: clusters: individual: Abell 2254 – Galaxies: clusters: general – Galaxies: kinematics and dynamics – X-rays: galaxies:clusters

1. Introduction

Merging processes constitute an essential ingredient of the evolution of galaxy clusters (see Feretti et al. 2002b for a review). An interesting aspect of these phenomena is the possible connection between cluster mergers and extended, diffuse radio sources: halos and relics. The synchrotron radio emission of these sources demonstrates the existence of large-scale cluster magnetic fields and of widespread relativistic particles. Cluster mergers have been proposed to provide the large amount of energy necessary for electron re-acceleration to relativistic energies and for magnetic field amplification (Tribble 1993; Feretti 1999; Feretti 2002a; Sarazin 2002). Radio relics ("radio gischts" as referred to by Kempner et al. 2004), which are polarized and elongated radio sources located in the cluster peripheral regions, seem to be directly associated with merger shocks (e.g., Ensslin et al. 1998; Roettiger et al. 1999; Ensslin & Gopal-Krishna 2001; Hoeft et al. 2004). Radio halos are unpolarized sources that per-

meate the cluster volume in a similar way to the X-ray emitting gas of the intracluster medium (hereafter ICM). Radio halos are more likely to be associated with the turbulence following a cluster merger, although the precise radio formation scenario remains unclear (re-acceleration vs. hadronic models e.g., Brunetti et al. 2009; Ensslin et al. 2011). Recent semi-analytical calculations in the framework of the turbulent re-acceleration scenario have allowed to derive the expectations for the statistical properties of giant radio halos, in agreement with present observation that halos are found in very massive clusters (Cassano & Brunetti 2005; Cassano et al. 2006). Very recently, a unified halo-relic model has been presented in the framework of hadronic models where the time-dependence of the magnetic fields and of the cosmic ray distributions is taken into account to explain the observational properties of both halos and (most) relics (Keshet 2010). In this model the ICM magnetization is triggered by a merger event, in part but probably not exclusively in the wake of merger shocks.

Unfortunately, one has been able to study these phenomena only recently on the basis of a sufficient statistics, i.e. few dozen clusters hosting diffuse radio sources up to $z \sim 0.5$ (e.g., Giovannini et al. 1999; see also Giovannini & Feretti 2002; Feretti 2005; Venturi et al. 2008; Bonafede et al. 2009; Giovannini et al. 2009). It is expected that new radio telescopes will largely increase the statistics of diffuse sources (e.g., LOFAR, Cassano et al. 2010a) and allow the study of diffuse radio emission in low X-ray luminosity clusters to discriminate among theories of halo formation (e.g., Cassano et al. 2005; Ensslin et al. 2011). The study of galaxy clusters with radio emission offers a unique tool to estimate strength and structure of large-scale magnetic fields and might have important cosmological implications (see Dolag et al. 2008 and Ferrari et al. 2008 for recent reviews). In particular, the study of clusters with radio halos/relics will likely contribute to quantify the effect of the non-thermal pressure to the estimate of mass and temperature in galaxy clusters (e.g., Loeb & Mao 1994; Markevitch 2010) and, more in general, the thermal and non thermal effects of cluster mergers on global properties and cosmological parameters (e.g., Sarazin 2004).

From the observational point of view, there is growing evidence of the connection between diffuse radio emission and cluster mergers, since up to now diffuse radio sources have been detected only in merging systems (see Cassano et al. 2010b). In most cases the cluster dynamical state has been derived from X-ray observations (Schuecker et al. 2001; Buote 2002; Cassano et al. 2010b). Optical data are a powerful way to investigate the presence and the dynamics of cluster mergers, too (e.g., Girardi & Biviano 2002). The spatial and kinematical analysis of member galaxies allow us to reveal and measure the amount of substructure, and to detect and analyze possible pre-merging clumps or merger remnants. This optical information is really complementary to X-ray information since galaxies and the ICM react on different timescales during a merger (see, e.g., the numerical simulations by Roettiger et al. 1997). In this context, we are conducting an intensive observational and data analysis program to study the internal dynamics of clusters with diffuse radio emission by using member galaxies (DARC – Dynamical Analysis of Radio Clusters – project, see Girardi et al. 2007[1]).

During our observational program, we have conducted an intensive study of the cluster Abell 2254 (hereafter A2254). A2254 is a very rich, X-ray luminous cluster: Abell richness

class = 2 (Abell et al. 1989); $L_X(0.1–2.4 \text{ keV})=7.19\times10^{44} h_{50}^{-2}$ erg s^{-1} (Ebeling et al. 1996). Optically, the cluster is classified as a Rood-Sastry morphological type "B", i.e. binary (Struble & Rood 1987). The cluster redshift reported in the literature refers to that $z = 0.178$ of the brightest cluster galaxy (Crawford et al. 1995).

Evidence for the existence of an extended, diffuse radio source was reported by Owen et al. (1999) and the presence of a radio halo, having a projected size of $\sim 5'$, is unambiguously shown by Giovannini et al. (1999). Both the radio and the X-ray emission (VLA 1.4 GHz and ROSAT HRI data, respectively) show a very clumpy and irregular structure (Govoni et al. 2001b), with a radio power at 1.4 GHz of $P_{1.4GHz} = 2.9\times10^{24} h_{70}^{-2}$ W Hz^{-1} and a large linear size of $\sim 0.9 h_{70}^{-1}$ Mpc.

We included this cluster in our DARC sample and obtained new spectroscopic and photometric data from the Telescopio Nazionale Galileo (TNG) and the Isaac Newton Telescope (INT), respectively. Our present analysis is based on these optical data, Subaru imaging data and XMM-Newton Science Archive data, too.

This paper is organized as follows. We present optical data and the cluster catalog in Sect. 2. We present our results about the cluster structure based on optical and X-ray data in Sects. 3 and 4, respectively. We discuss our results and present our conclusions in Sect. 5.

Unless otherwise stated, we indicate errors at the 68% confidence level (hereafter c.l.). Throughout this paper, we use $H_0 = 70$ km s^{-1} Mpc^{-1} and $h_{70} = H_0/(70 \text{ km s}^{-1} \text{ Mpc}^{-1})$ in a flat cosmology with $\Omega_0 = 0.3$ and $\Omega_\Lambda = 0.7$. In the adopted cosmology, $1'$ corresponds to $\sim 180 h_{70}^{-1}$ kpc at the cluster redshift.

2. Galaxy data and catalog

2.1. Spectroscopic observations

Multi-object spectroscopic observations of A2254 were carried out at the TNG telescope in May/October 2009 and in March 2010. We used DOLORES/MOS with the LR-B Grism 1, yielding a dispersion of 187 Å/mm. We used the 2048 × 2048 pixels E2V CCD, with a pixel size of 13.5 μm. In total, we observed 4 MOS masks for a total of 142 slits. Total exposure times were 3600 s for two masks and 5400 s for the other two masks.

Wavelength calibration was performed using helium and neon-mercury lamps. Reduction of spectroscopic data was carried out using the IRAF[2] package. Radial velocities were determined using the cross-correlation technique (Tonry & Davis 1979) implemented in the RVSAO package (developed at the Smithsonian Astrophysical Observatory Telescope Data Center). Each spectrum was correlated against five templates for a variety of galaxy spectral types: E, S0, Sa, Sb, and Sc (Kennicutt 1992). The template producing the highest value of $\mathcal{R}$, i.e., the parameter given by RVSAO and related to the signal-to-noise ratio of the correlation peak, was chosen. Moreover, all spectra and their best correlation functions were examined visually to verify the redshift determination. In three cases (IDs. 24, 35 and 60; see Table 1), we assumed the EMSAO redshift to be a reliable estimate of the redshift. Our spectroscopic catalog lists 128 galaxies in the field of A2254.

The formal errors as given by the cross-correlation are known to be smaller than the true errors (e.g., Malumuth et al. 1992; Bardelli et al. 1994; Ellingson & Yee 1994; Quintana et al. 2000). Duplicate observations for the same galaxy allowed us to estimate the true intrinsic errors in data of the same quality taken with the same instrument (e.g. Barrena et al. 2009). Here we have double determinations for seven galaxies, thus we decided to apply the procedure that had already been applied in the above study obtaining that true errors are larger than formal cross-correlation errors by a factor of 2.2. For the seven galaxies with two redshift estimates, we used the mean of the two measurements and the corresponding errors. As for the radial velocities estimated through EMSAO we assumed the largest between the formal error and 100 km s^{-1}. As for the whole catalog, the median value of the cz errors, taking into account the above correction, is 66 km s^{-1}.

2.2. INT observations

Our photometric observations were carried out with the Wide Field Camera (WFC), mounted at the prime focus of the 2.5m INT telescope. We observed A2254 in g', r' and i' SDSS filters in photometric conditions and a seeing of ~1.6″.

The WFC consists of a four-CCD mosaic covering a 33′×33′ field of view, with only a 20% marginally vignetted area. We took twelve exposures of 600 s in g' filter, nine exposures of 450 s in r' filter and nine exposures of 400 s in i' filter. So a total of 7200 s in g' filter, 4050 s in r' and 3600 s in i' band. The observations were performed making a dithering pattern. This observing procedure allowed us to build a "supersky" frame that was used to correct our images for fringing patterns (Gullixson 1992). In addition, the dithering helped us to clean cosmic rays and avoid the effects of gaps between the CCDs in the final full mosaic images. Another problem associated with the wide field frames is the distortion of the field. To match the photometry of several filters, a good astrometric solution is needed to take into account these distortions. Using the *imcoords* IRAF tasks and taking as a reference the USNO B1.0 catalog, we were able to find an accurate astrometric solution (rms ~0.3″) across the full frame. Only in the North-East edge of the image, at ~17′ from the cluster center, we could not obtain a sufficiently good astrometric solution. In order to guarantee a good match between g', r' and i' catalogs, this marginal region was removed from the master catalog. The photometric calibration was performed by observing the SA108 standard Landolt field (Landolt 1992) that is also calibrated in the SDSS photometric system (Smith 2002).

We finally identified galaxies in our g', r' and i' images and measured their magnitudes with the SExtractor package (Bertin & Arnouts 1996) and AUTOMAG procedure. Objects were identified by imposing that they cover a certain minimum area and have a number of counts above a limiting threshold taking the sky local background as a reference. The limiting size and flux were 16 pixels and 1.5 standard deviation above the sky counts level, respectively. The selected limiting size corresponds to an apparent size of 1.3″, which is about the minimum seeing size during the observations. We also performed visual inspections of the frames in order to deal with the best combination of the above parameters that remove spurious objects from the catalogs.

In a few cases (e.g., close couples of galaxies, galaxies very close to bright stars or close to defects of the CCD) the standard SExtractor photometric procedure failed. In these cases, we computed magnitudes by hand. This method consisted of measuring fluxes assuming a galaxy profile of a typical elliptical

galaxy and scaling it to the maximum observed value. The integration of this profile provided an estimate of the magnitude. This method is similar to PSF photometry, but assumes an E-type galaxy profile, which is more appropriate in this case.

As a final step, we estimated and corrected the Galactic extinction $A_{g'} \sim 0.21$, $A_{r'} \sim 0.15$ and $A_{i'} \sim 0.10$ using Schlegel et al. (1998) reddening and extinction maps computed from IRAS and COBE/DIRBE data. We estimated that our photometric sample is complete down to $g' = 23.4$ (24.3), $r' = 22.1$ (23.3) and $i' = 21.9$ (23.3) for $S/N = 5$ (3) within the observed field. We assigned magnitudes to all galaxies of our spectroscopic catalog.

2.3. Subaru images

Subaru Suprime-Cam data were retrieved from the SMOKA archive[3]. Following the same steps adopted by Nonino et al. (2009), the images in V-band and i'-band were coadded and reduced to cover a 30′×30′ field of view. Seeing conditions were ~ 0.8″– 1.0″, with a total exposure time of 1200s in V-band, and 1920s in i'-band. The astrometric solutions were obtained using 2MASS as reference.

Unfortunately, the observations in both filters were collected under non-photometric conditions, as shown from the relative photometric analysis. Therefore, the final coadded images were not calibrated using standard stars. For the use we make in this study, i.e. the 2D analysis of substructure, non calibrated magnitudes are quite sufficient and we refer them as i'_{obs} and V_{obs} (see Sect. 3.4 for other details).

2.4. Galaxy catalog

Table 1 lists the velocity catalog (see also Fig. 2): identification number of each galaxy and member galaxies, ID and IDm (Cols. 1 and 2, respectively); right ascension and declination, α and δ (J2000, Col. 3); g', r', and i' INT magnitudes (Cols. 4, 5 and 6); heliocentric radial velocities, v = $cz_{\odot}$ (Col. 7) with errors, Δv (Col. 8).

2.5. Individual galaxies

No evident dominant galaxy is present in the cluster since the brightest galaxy in our catalog (ID. 53, $r' = 16.22$, hereafter BCG) is less than 0.5 mag brighter then the following brightest galaxies (IDs. 117, 102, 112 with $r' = 16.64$, 16.66, and 16.67 respectively). These bright galaxies all lie in the eastern region of the cluster; we refer to them as BCG2, BCG3, and BCG4.

The BCG is close to the peak of the X-ray emission and has a (projected) bright companion ($r' = 17.01$, ID. 50 hereafter BCGc). BCGc is characterized by [OII], Hβ, and [OIII] emission spectral lines, strong 24μ MIPS-Spitzer emission[4], UV emission[5], and faint radio emission (ID. 2 in Table 3 of Rizza et al. 2003). The Subaru images show that it is a spiral galaxy with a large bulge and an arm directed toward the BCG (see Fig. 3). We find a quite large relative velocity difference with respect to the BCG (~ 1400 km s^{-1}).

Figure 2 of Govoni et al. (2001b) suggests the presence of a few discrete radio sources. The brightest one – with a flux of ~ 38 mJy at 1.4 GHz – lies in the NE cluster region where the field is very crowded. The likely optical counterpart might be the cluster galaxy ID. 93 (hereafter "RG") which has an optical

Table 1. Velocity catalog of 128 spectroscopically measured galaxies in the field of the cluster A2254.

Table 1. Continued.

ID	IDm	α, δ (J2000)	g'	r'	i'	v (km s^{-1})	Δv
1	1	17 17 24.62, +19 41 59.6	18.52	17.45	16.98	51510	53
2	2	17 17 25.92, +19 39 54.7	20.72	19.63	19.25	52688	68
3	–	17 17 25.97, +19 43 25.3	18.62	17.27	16.84	72033	64
4	–	17 17 26.26, +19 42 20.5	18.90	17.70	17.41	70536	66
5	3	17 17 26.59, +19 41 31.6	18.89	18.17	17.96	52741	77
6	4	17 17 27.62, +19 42 14.8	19.31	18.15	17.74	52931	46
7	–	17 17 28.94, +19 40 18.1	21.59	20.08	19.37	165420	106
8	5	17 17 30.10, +19 43 30.0	19.88	18.71	18.30	53232	70
9	6	17 17 31.68, +19 42 06.1	19.28	18.16	17.76	53803	55
10	–	17 17 32.35, +19 43 13.4	20.82	19.89	19.46	78076	84
11	7	17 17 33.53, +19 41 07.1	19.68	19.11	18.99	53136	90
12	–	17 17 33.55, +19 42 42.1	20.26	19.21	18.94	71797	64
13	–	17 17 34.37, +19 42 48.6	17.50	16.51	16.12	36622	37
14	8	17 17 35.35, +19 42 42.8	19.70	18.87	18.56	54559	103
15	9	17 17 35.95, +19 39 27.4	20.10	19.10	18.81	52006	139
16	10	17 17 36.43, +19 41 07.8	19.71	18.67	18.32	51360	42
17	11	17 17 36.46, +19 39 02.2	19.32	18.57	18.26	54600	73
18	12	17 17 36.74, +19 42 03.6	20.80	19.65	19.28	54105	70
19	13	17 17 37.03, +19 41 11.4	19.44	18.75	18.35	53377	53
20	–	17 17 37.87, +19 41 17.9	21.04	19.72	19.36	62831	62
21	–	17 17 38.04, +19 40 04.4	20.20	18.95	18.72	70432	46
22	14	17 17 38.04, +19 44 55.7	20.37	19.27	18.89	55154	101
23	15	17 17 38.21, +19 40 03.7	21.76	20.84	19.88	52576	150
24	16	17 17 38.26, +19 38 46.3	21.17	20.03	19.47	53964	100
25	17	17 17 38.95, +19 40 01.6	19.37	18.20	17.79	52664	62
26	–	17 17 39.10, +19 41 33.0	21.20	19.77	19.21	149288	48
27	18	17 17 39.65, +19 41 06.7	20.22	19.05	18.79	51500	121
28	19	17 17 39.70, +19 38 02.8	20.52	19.45	19.07	54068	63
29	20	17 17 39.84, +19 38 10.7	20.67	19.64	19.30	52684	90
30	21	17 17 39.84, +19 38 10.7	20.67	19.64	19.30	54818	90
31	22	17 17 40.03, +19 40 52.0	19.43	18.35	17.98	52821	33
32	23	17 17 40.63, +19 37 42.6	20.52	19.86	19.63	51947	240
33	24	17 17 40.66, +19 41 40.9	20.33	19.16	18.70	54364	66
34	25	17 17 40.68, +19 39 52.2	20.98	19.84	19.39	54308	103
35	26	17 17 41.02, +19 43 53.8	20.16	19.37	19.06	51559	100
36	27	17 17 41.33, +19 39 52.2	19.78	19.06	18.81	53081	128
37	–	17 17 41.38, +19 41 42.0	18.73	18.04	17.75	62608	55
38	28	17 17 41.57, +19 41 07.4	19.01	18.04	17.81	54845	66
39	29	17 17 42.34, +19 42 39.2	17.98	17.18	16.90	54521	77
40	30	17 17 43.01, +19 42 26.3	19.19	18.05	17.58	53870	62
41	31	17 17 43.06, +19 41 44.2	18.91	17.98	17.57	52292	35
42	32	17 17 43.06, +19 43 51.6	18.75	17.69	17.41	53468	41
43	33	17 17 43.20, +19 44 59.6	19.16	18.28	17.99	50532	51
44	34	17 17 43.61, +19 39 20.5	19.25	18.10	17.77	52880	66
45	35	17 17 43.61, +19 42 42.1	19.58	18.47	18.09	53563	44
46	36	17 17 43.63, +19 38 37.7	21.34	20.46	20.07	51447	99
47	37	17 17 43.70, +19 39 24.8	20.90	19.97	19.65	52533	189
48	38	17 17 43.80, +19 41 12.1	19.26	18.24	17.96	55744	62
49	39	17 17 43.87, +19 41 43.4	19.42	18.10	17.93	52024	66
50	40	17 17 45.53, +19 40 40.1	17.90	17.01	16.74	54579	53
51	41	17 17 45.62, +19 41 57.1	21.28	20.09	19.72	53513	110
52	42	17 17 45.65, +19 38 13.6	19.31	18.33	17.93	53918	66
53	43	17 17 45.86, +19 40 48.4	17.44	16.22	15.73	52963	41
54	44	17 17 45.86, +19 41 47.4	19.69	18.62	18.23	51347	55
55	45	17 17 45.86, +19 40 45.8	20.66	19.76	19.21	53276	75
56	46	17 17 45.91, +19 39 41.4	19.45	18.29	17.89	53264	44
57	47	17 17 46.30, +19 42 20.9	20.35	19.24	18.84	52108	130
58	48	17 17 46.51, +19 42 42.5	20.45	19.49	19.01	53167	59
59	49	17 17 46.58, +19 40 05.9	19.90	19.27	18.40	53069	55
60	–	17 17 46.75, +19 40 30.7	19.43	18.83	18.58	23305	170
61	50	17 17 46.97, +19 39 31.3	18.94	17.81	17.36	50067	66
62	–	17 17 47.59, +19 41 29.4	20.50	19.78	19.51	89174	158
63	51	17 17 47.69, +19 44 15.4	19.27	18.46	18.20	55316	66
64	52	17 17 47.78, +19 41 35.9	19.13	18.14	17.80	54202	59
65	53	17 17 47.95, +19 37 00.8	20.57	19.49	19.07	55387	59
66	54	17 17 48.02, +19 38 51.4	20.31	19.28	18.92	55179	46
67	55	17 17 49.78, +19 41 10.7	19.82	18.87	18.55	54240	77
68	56	17 17 49.82, +19 41 18.2	21.19	20.17	19.85	51305	114
69	57	17 17 50.02, +19 39 07.6	18.15	16.98	16.57	54695	39
70	58	17 17 50.81, +19 41 43.4	18.86	17.76	17.35	51441	37
71	59	17 17 50.95, +19 41 12.5	20.47	19.41	19.28	53289	55
72	60	17 17 51.22, +19 42 38.5	18.84	18.06	17.84	49237	79
73	61	17 17 51.48, +19 40 36.1	19.47	18.31	17.95	52695	79
74	–	17 17 51.58, +19 42 52.9	18.61	17.37	16.94	62934	70
75	62	17 17 51.65, +19 41 20.4	19.78	18.57	18.70	51961	86
76	63	17 17 52.13, +19 40 19.6	19.39	18.26	17.85	52167	59
77	64	17 17 52.61, +19 40 08.0	20.18	19.04	18.76	52308	46
78	65	17 17 53.04, +19 44 24.0	19.94	18.82	18.45	51433	66
79	66	17 17 53.21, +19 38 47.8	18.73	17.68	17.34	50868	46
80	67	17 17 53.52, +19 40 25.0	20.20	19.10	18.68	56052	86
81	68	17 17 54.12, +19 41 47.8	19.13	18.00	17.64	52069	48
82	69	17 17 54.17, +19 43 36.1	21.78	20.77	20.30	53213	108
83	70	17 17 54.84, +19 38 14.3	19.58	18.70	18.37	53855	64
84	71	17 17 54.91, +19 39 04.3	20.28	19.16	18.74	53449	75

spectrum typical of ellipticals. ID. 93, with an absolute magnitude $M_R \sim -21.9$ and a radio power $\log P_{1.4GHz}(\text{W Hz}^{-1}) \sim 24.5$, can be accommodated among the radio galaxies in clusters (e.g., Ledlow & Owen 1996; Bardelli et al. 2010). However, a very faint, extended object close to RG is revealed by the Subaru image (Fig. 4). Due to the present resolution in radio data, there is some doubt on the identification of RG as the (unique) responsible of the whole radio emission of the bright discrete radio source. Figure 4 also shows the position of a point-like X-ray source and of a MIPS-Spitzer source.

A full discussion of individual galaxies is far from the aim of this study and we only give Figs. 3 and 4 in the electronic version of the paper.

3. Analysis of the optical data
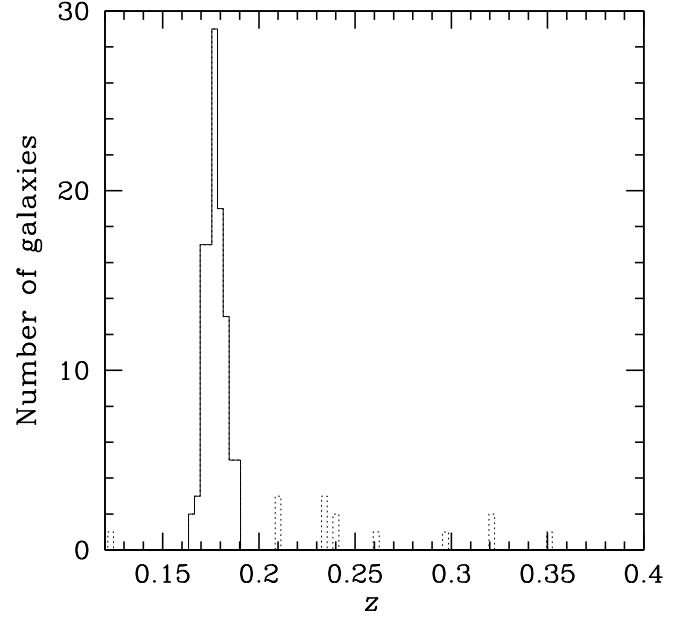
3.1. Member selection

To select cluster members among the 128 galaxies with redshifts we perform the 1D adaptive-kernel method (hereafter DEDICA, Pisani 1993 and 1996; see also Fadda et al. 1996; Girardi et al. 1996). We search for significant peaks in the velocity distribution at >99% c.l.. This procedure detects A2254 as a peak at $z \sim 0.177$ populated by 110 galaxies considered as fiducial cluster members (in the range $49\,237 \leq v \leq 56\,757$ km s^{-1}, see Fig. 5). As for the center of A2254, we adopt the position of the BCG [R.A.=$17^h17^m45\overset{s}{.}86$, Dec.=+19°40′48.4″ (J2000.0)]. The 18 non-members are 2 and 16 foreground and background galaxies, respectively.

In the previous analyses of DARC clusters we generally used a second step in the member selection, which uses the combina-

Table 1. Continued.

ID	IDm	α, δ (J2000)	g'	r'	i'	v (km s^{-1})	Δv
85	72	17 17 54.96, +19 39 29.2	20.38	19.87	19.61	54529	174
86	73	17 17 55.06, +19 40 16.0	18.56	17.49	17.11	49834	62
87	74	17 17 55.06, +19 42 10.8	20.40	19.22	18.82	56376	66
88	75	17 17 55.08, +19 41 10.7	19.59	18.40	17.99	56400	48
89	76	17 17 55.46, +19 37 52.0	21.36	20.34	19.98	53505	101
90	77	17 17 55.75, +19 41 53.2	20.84	19.94	19.64	56368	97
91	78	17 17 55.78, +19 39 41.4	19.97	18.83	18.44	56515	59
92	79	17 17 55.78, +19 40 36.8	19.18	18.60	18.37	52917	68
93	80	17 17 56.02, +19 40 59.5	18.93	17.81	17.41	53106	53
94	81	17 17 56.09, +19 42 14.4	20.78	19.93	19.98	51396	75
95	82	17 17 56.30, +19 39 54.4	19.64	18.49	18.05	51354	37
96	83	17 17 56.42, +19 41 43.4	20.13	19.15	18.82	55943	117
97	84	17 17 56.50, +19 37 59.9	20.34	19.25	18.86	53815	57
98	85	17 17 56.62, +19 42 56.5	19.35	18.18	17.82	54648	35
99	86	17 17 56.95, +19 41 21.5	19.97	18.92	18.59	54154	44
100	87	17 17 57.07, +19 41 28.7	18.67	17.54	17.16	53106	42
101	88	17 17 57.19, +19 37 23.5	20.86	19.86	19.61	52885	97
102	89	17 17 57.26, +19 39 35.3	17.79	16.66	16.25	51409	55
103	90	17 17 57.29, +19 41 52.4	18.92	17.78	17.38	52138	42
104	91	17 17 57.53, +19 43 52.0	18.91	17.75	17.59	53675	51
105	92	17 17 57.67, +19 43 42.2	19.98	19.06	19.05	53747	79
106	93	17 17 57.84, +19 43 28.9	19.01	18.45	18.17	54201	68
107	94	17 17 58.13, +19 38 39.1	18.47	17.59	17.41	50570	55
108	95	17 17 58.20, +19 36 45.7	20.65	19.54	19.23	51708	62
109	–	17 17 58.20, +19 40 36.5	20.34	19.60	19.20	96562	147
110	96	17 17 59.21, +19 37 23.2	19.97	18.93	18.59	51871	70
111	97	17 17 59.21, +19 40 45.1	19.34	18.19	17.73	56757	55
112	98	17 17 59.69, +19 40 25.7	17.77	16.67	16.26	53416	64
113	99	17 17 59.83, +19 42 09.0	19.57	18.92	18.70	51016	57
114	100	17 17 59.98, +19 40 54.1	20.66	19.89	19.57	53090	68
115	101	17 18 00.58, +19 43 44.8	20.94	20.04	19.64	52104	90
116	102	17 18 00.67, +19 40 00.1	20.92	19.80	19.40	54904	77
117	103	17 18 01.30, +19 40 58.4	17.74	16.64	16.21	54229	57
118	104	17 18 01.70, +19 39 28.8	19.27	18.13	17.72	52903	68
119	105	17 18 01.97, +19 40 22.4	19.56	18.53	18.08	51933	92
120	–	17 18 01.99, +19 37 56.6	20.09	19.31	18.97	70025	99
121	106	17 18 03.31, +19 42 09.4	19.80	18.70	18.34	55067	46
122	107	17 18 03.46, +19 36 14.0	20.19	19.12	18.73	51813	64
123	–	17 18 03.62, +19 37 33.6	21.07	19.97	19.51	122887	200
124	108	17 18 04.46, +19 40 21.4	19.72	19.58	19.50	50836	110
125	–	17 18 04.61, +19 39 22.3	19.71	18.28	17.80	105488	55
126	109	17 18 06.00, +19 39 55.1	19.51	18.52	18.17	52452	125
127	110	17 18 06.05, +19 38 17.5	18.38	17.29	16.90	51558	62
128	–	17 18 07.51, +19 37 40.8	19.72	18.71	18.36	96285	75

Fig. 5. Redshift galaxy distribution. The solid line histogram refers to the 110 galaxies assigned to A2254 according to the DEDICA reconstruction method.

tion of position and velocity information, i.e., the "shifting gapper" method by Fadda et al. (1996). This procedure rejects galaxies that are too far in velocity from the main body of galaxies within a fixed bin that shifts along the distance from the cluster center (adopted values are 1000 km s^{-1} in the cluster rest-frame for the velocity cut and 0.6 h_{70}^{-1} Mpc, or large enough to include 15 galaxies, for the spatial shifting bin). The procedure is iterated until the number of cluster members converges to a stable value (see Fadda et al. for other details and their Fig. 1 for an example). Here, the formal application of the "shifting gapper" procedure would reject another four galaxies just at the border of the distribution of galaxies in the plane of the rest-frame velocity vs. projected clustercentric distance (see the crosses in the Fig. 6 – top panel). These galaxies are not spatially clustered and

have the typical early-type galaxy colors. Therefore, we decide to not reject them from the analysis. Global cluster quantities are independent of this decision within the 1σ error. Note that the "shifting gapper" procedure is completely empirical and has the advantage of being independent of hypotheses about the poorly known dynamical status of the cluster. Other available procedures combining position and velocity information are generally based on physical assumptions about the dynamical status of the cluster and the consequent possibility to apply the virial mass and/or the knowledge of the mass profile (e.g., den Hartog & Katgert 1996, see Biviano et al. 2006 for a recent application). Therefore, the application of these procedures is not well justified in the case of A2254 showing evidence of substructure (see in the following). Making an attempt in this direction, we use the value of the mass obtained in Sect. 5.3, $M_{\rm sys}$, and adopt a one-single cluster model described by the NFW mass profile (Navarro et al. 1997, see Sect. 5.3 too) to construct the upper limits to the LOS velocities at projected distance R from the cluster center (criterion (i) by den Hartog & Katgert 1996). Figure 6 shows as the region of allowed velocities is roughly coincident with that occupied by our selected member galaxies. Thus, although in the case of the substructured cluster A2254 we do not expect to determine the detailed cluster membership, it supports the consistency between our adopted galaxy membership and the value we obtain for the mass estimate.
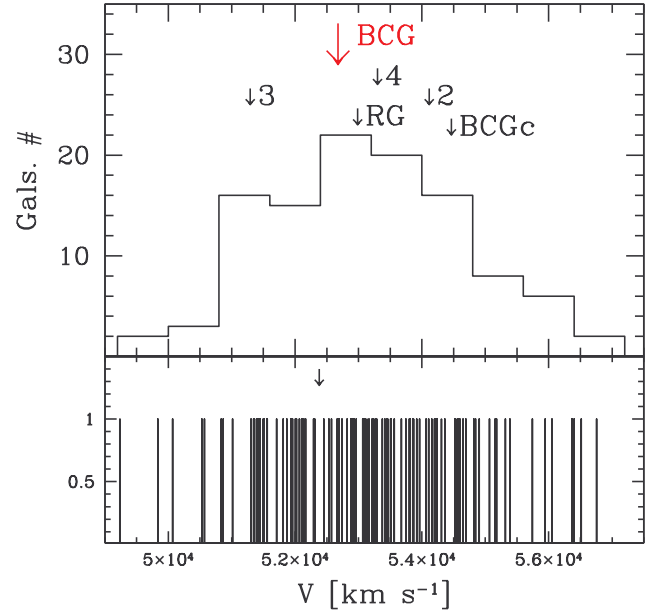
3.2. Global cluster properties

By applying the biweight estimator to the 110 cluster members (Beers et al. 1990, ROSTAT software), we compute a mean cluster redshift of $\langle z \rangle = 0.1772 \pm 0.0004$, i.e. $\langle v \rangle = (53\,128 \pm 125)$ km s^{-1}. We estimate the LOS velocity dispersion, σ_V, by using the biweight estimator and applying the cosmological correction and the standard correction for velocity errors (Danese
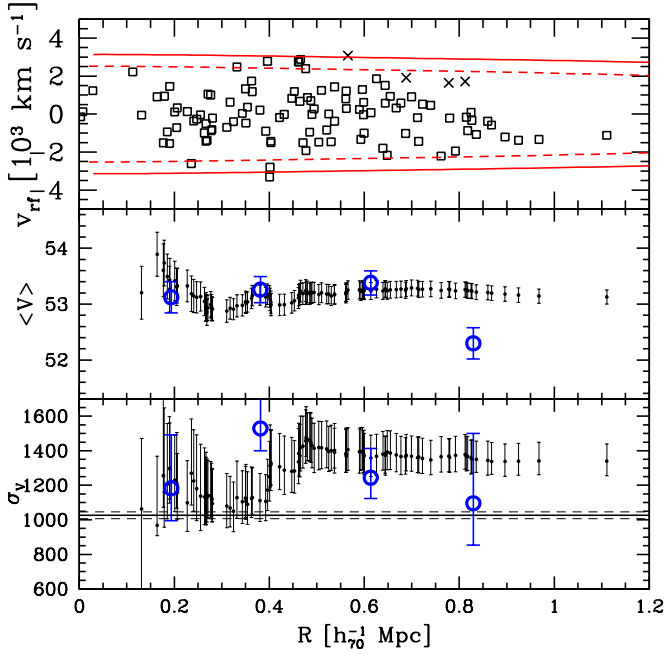
Fig. 6. *Top panel:* rest-frame velocity vs. projected clustercentric distance for the 110 member galaxies of the fiducial sample (Fig. 5). Crosses indicate galaxies formally rejected as interlopers by the "shifting gapper" procedure, but here considered in a more conservative view. The cluster center coincides with the position of the BCG. Red solid (dashed) curves enclose the region of allowed values for member galaxies according to the criterion of den Hartog & Katgert (1996) and using the upper (lower) limit of our mass estimate computed in the following (see Sect. 5.3). *Middle and bottom panels:* differential (big circles) and integral (small points) profiles of mean velocity and LOS velocity dispersion, respectively. For the differential profiles, we plot the values for four annuli from the center of the cluster, each of 0.25 h_{70}^{-1} Mpc (large blue symbols). For the integral profiles, the mean and dispersion at a given (projected) radius from the cluster-center is estimated by considering all galaxies within that radius – the first value computed on the five galaxies closest to the center. The error bands at the 68% c.l. are also shown. In the bottom panel, the horizontal line represents the X-ray temperature with the respective errors transformed in σ_V assuming the density-energy equipartition between ICM and galaxies, i.e. $\beta_{spec} = 1$ (see Sect. 5).

Fig. 7. The 110 galaxies assigned to the cluster. *Upper panel:* Velocity distribution. The arrows indicate the velocities of the BCG, other brightest galaxies, and RG. *Lower panel:* Stripe density plot where the arrow indicates the position of the significant gap.
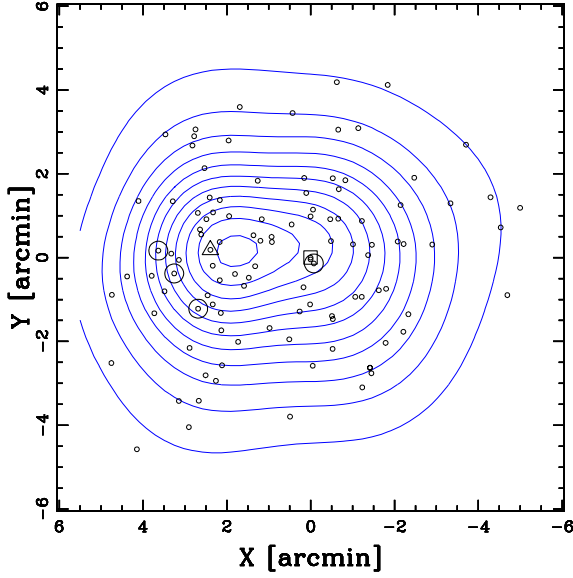
3.3. Velocity distribution

We analyze the velocity distribution to search for possible deviations from Gaussianity that might provide important signatures of complex dynamics. For the following tests, the null hypothesis is that the velocity distribution is a single Gaussian.

We estimate three shape estimators, i.e., the kurtosis, the skewness, and the scaled tail index (see, e.g., Bird & Beers 1993). There is no evidence of departures from the Gaussianity (see Table 2 of Bird & Beers 1993).

We then investigate the presence of gaps in the velocity distribution. We follow the weighted gap analysis presented by Beers et al. (1991; 1992; ROSTAT software). We look for normalized gaps larger than 2.25 since in random draws of a Gaussian distribution they arise at most in about 3% of the cases, independent of the sample size (Wainer and Schacht 1978). We detect one significant gap (at the 97% c.l.), which divide the cluster into two groups of 36 and 70 galaxies from low to high velocities (hereafter GV1 and GV2, see Fig. 7). The BCG3 is assigned to the GV1 peak. Other bright galaxies (BCG, BCG2, BCG4, and BCGc) are all assigned to the GV2 peak.

To detect subsets in the velocity distribution we then resort to the Kaye's mixture model (KMM) test (Ashman et al. 1994). The KMM algorithm fits a user-specified number of Gaussian distributions to a dataset and assesses the improvement of that fit over a single Gaussian. In addition, it provides the maximum-likelihood estimate of the unknown n-mode Gaussians and an assignment of objects into groups. The KMM test is more appropriate in situations where theoretical and/or empirical arguments indicate that a Gaussian model is reasonable. The Gaussian is valid in the case of cluster velocity distributions, where gravitational interactions drive the system toward a relaxed configuration with a Gaussian velocity distribution. The KMM test does not find a two-group partition, which provides a significantly

et al. 1980). We obtain $\sigma_V = 1340_{-84}^{+101}$ km s^{-1}, where errors are estimated through a bootstrap technique.

To evaluate the robustness of the σ_V estimate, we analyze the velocity dispersion profile (Fig. 6). The integral profile shows an enhancement at ~ 0.4–0.5 h_{70}^{-1} Mpc from the cluster center and then flattens. This suggests that a robust value of σ_V is asymptotically reached in the external cluster regions, as found for most nearby clusters (e.g., Fadda et al. 1996; Girardi et al. 1996). As for the enhancement at ~ 0.4–0.5 h_{70}^{-1} Mpc, it is likely due to the contamination of the galaxies of a secondary clump (see Sects. 3.4 and 3.5); see also, e.g., Girardi et al. (1996) and Barrena al. (2007) for examples in other clusters).

Fig. 8. Spatial distribution on the sky and relative isodensity contour map of spectroscopic cluster members, obtained with the 2D-DEDICA method. The BCG is taken as the cluster center. Large square and circles indicate the location of the BCG and other brightest galaxies. Large triangle indicates RG.

more accurate description of the velocity distribution than a single Gaussian.

To search for a possible physical meaning of the two subclusters determined by the detected significant velocity gap, we also compare two by two the spatial galaxy distributions of GV1 and GV2. We find no difference according to the the 2D Kolmogorov-Smirnov test (Fasano 1987).

3.4. Analysis of the 2D galaxy distribution

By applying the 2D adaptive-kernel method (2D-DEDICA) to the positions of A2254 galaxy members, we find one peak which is ~ 2′ far East from the position of the BCG and the isodensity contours design a E-W elongated structure. (Fig. 8).

Our spectroscopic data do not cover the entire cluster field and are affected by magnitude incompleteness. To overcome these problems, we use our photometric data samples which cover a larger spatial region. The INT sample has the advantage to have photometry available in three magnitude bands, while the Subaru sample allows us to extend our analysis to fainter galaxies.

When more than two colors are available, it is more effective to select galaxies in the color-color space (Goto et al. 2002). In particular, Lu et al. (2009, see their Figs. 6 and 7) show as $(r'-i')$ color can effectively eliminate high redshift galaxies from the red-sequence galaxies at $z=0.2$–0.3 redshift. In our INT photometric catalog we select likely members on the basis of both $(r'-i'$ vs. $r')$ and $(g'-r'$ vs. $r')$ color-magnitude relations (hereafter CMRs), which indicate the early-type galaxies locus. To determine the CMR we apply the 2σ-clipping fitting procedure to the cluster members: we obtain $r'-i'=0.777-0.021\times r'$ and $g'-r'=1.497-0.021\times r'$ (see Fig. 9). Out of our photometric catalog we consider as likely "red" cluster members those objects lying within 0.1 and 0.15 mag of the CMRs $(r'-i'$ vs. $r')$ and $(g'-r'$ vs. $r')$, respectively. The selected magnitude intervals are chosen with different widths to follow the different amplitudes of
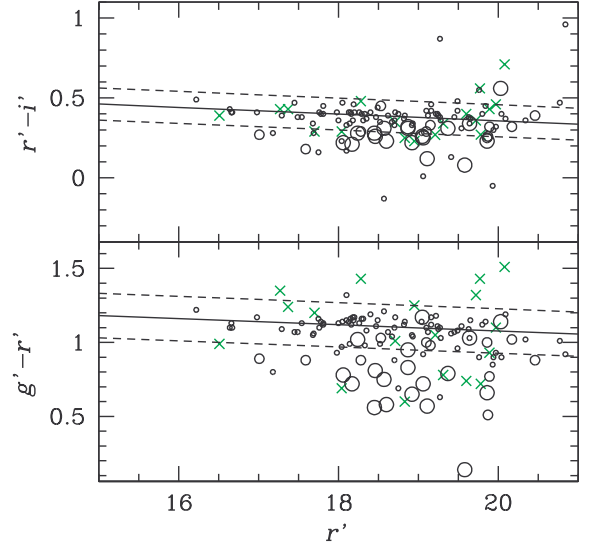
Fig. 9. *Upper panel:* INT $r' - i'$ vs. r' diagram for galaxies with available spectroscopy. Black circles and green crosses indicate member and no-member galaxies. For member galaxies large/middle/small size circles indicate late/middle/early type galaxies. The solid line gives the CMR determined on member galaxies; the dashed lines are drawn at ±0.1 mag from this value. *Lower panel:* INT $g' - r'$ vs. r' diagram for galaxies with available spectroscopy. The dashed lines are drawn at ±0.15 mag from the CMR determined on member galaxies.

the scatter in the two relations: 0.1 and 0.15 mag are round values roughly corresponding to ~ 1.3 times the error associated to the fitted intercepts. Note that the difference in the scatter between the two above CMRs is quite expected: for instance, using SDSS data, Goto et al. (2002) computed a scatter of 0.040 and 0.081 for the two above relations, respectively.

As a further check, we associate to each galaxy the galaxy type producing the highest value of $\mathcal{R}$ in the RVSAO procedure and divide galaxies in early-type (E, S0), middle-type (Sa, Sb), and late-type (Sc, Irr). The galaxies with z determined via EMSAO are assigned to late-type galaxies. Although these spectral-types do not pretend to be an alternative to a complete spectral analysis, they are useful to show how the selection through the CMR, in particular here the $(g'-r'$ vs. $r')$, is useful to distinguish between early and late-type galaxies (see Fig. 9 – lower panel). Figure 9 shows as the selected magnitude intervals seem adequate to select early-type galaxies, thus to only use good tracers of the cluster substructure (e.g., Lubin et al. 2000) and, above all, to avoid non-member galaxies which might bias our 2D analysis.
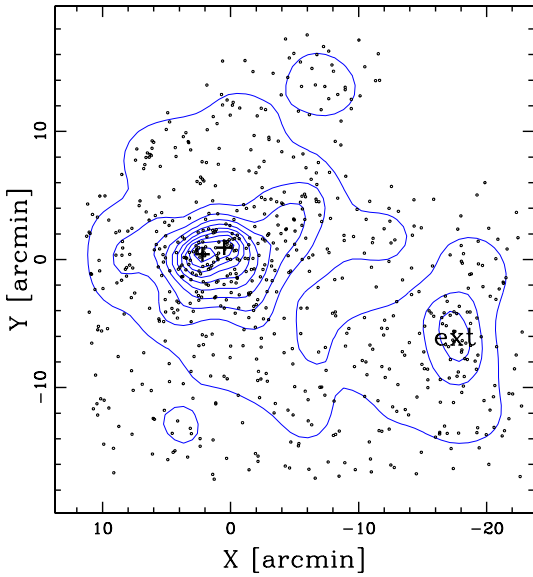
Figure 10 shows the contour map for the 682 likely cluster members having $r' \leq 21$. We find two, very significant peaks along the E-W direction, hereafter E- and W-peaks. The W-peak is at ~ 1′ north from the BCG. A third peak lies in the WSW region, where our photometric data allow to study very external cluster regions (hereafter ext-peak). Similar results are found for the 780 objects with $r' \leq 21.5$.

As for the results with $r' \leq 21$, Table 2 lists the number of assigned members, N_S (Col. 2); the peak position (Col. 3); the density (relative to the densest peak), ρ_S (Col. 4); the value of χ^2 for each peak, χ_S^2 (Col. 5). Ramella et al. (2007) tested the 2D-DEDICA procedure on Monte Carlo simulations reproduc-
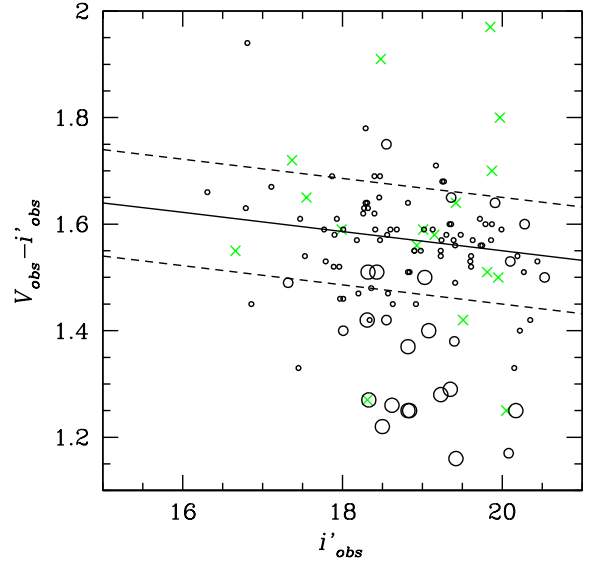
Table 2. 2D substructure from the INT and SUBARU photometric samples.

Subclump	N_S	α(J2000), δ(J2000) h : m : s, $^{\circ}$: $'$: $''$	ρ_S	χ_S^2
2D – E (INT $r' < 21$)	164	17 17 55.2 + 19 41 13	1.00	65
2D – W (INT $r' < 21$)	214	17 17 48.0 + 19 41 44	0.91	55
2D – ext (INT $r' < 21$)	159	17 16 31.4 + 19 34 48	0.33	44
2D – E (SUB $i' < 20.5$)	131	17 17 55.9 + 19 41 03	1.00	43
2D – W (SUB $i' < 20.5$)	248	17 17 46.8 + 19 41 07	0.94	46
2D – ext (SUB $i' < 20.5$)	159	17 16 38.0 + 19 35 33	0.37	33
2D – SW (SUB $i' < 21.5$)	122	17 17 47.0 + 19 40 53	1.00	37
2D – E (SUB $i' < 21.5$)	77	17 17 56.4 + 19 41 13	0.73	31
2D – NW (SUB $i' < 21.5$)	22	17 17 46.0 + 19 42 10	0.69	15
2D – ext (SUB $i' < 21.5$)	54	17 16 36.5 + 19 35 45	0.36	19

Fig. 11. Subaru $V_{obs} - i'_{obs}$ vs. i'_{obs} diagram for galaxies with available spectroscopy. Black circles and green crosses indicate member and no-member galaxies. For member galaxies large/middle/small size indicate late/middle/early type galaxies. The solid line gives the CMR determined on member galaxies; the dashed lines are drawn at ±0.1 mag from this value.

Fig. 10. Spatial distribution on the sky and relative isodensity contour map of INT photometric cluster members with $r' \leq 21$, obtained with the 2D-DEDICA method. The two crosses indicate the E- and W-peaks.

ing galaxy clusters. They show that the physical significance, i.e. the significance which takes into account the noise fluctuations, associated to the subclusters depends on the statistical significance of the subcluster (recovered from the χ^2 value) and can be computed using simulations. Considering their eq. 5, the χ^2 threshold for a sample of 682 objects is $\chi^2_{threshold}$ =32. Thus, all the three peaks we detect are physically significant.

In the Subaru photometric catalog we select likely members on the basis of the ($V_{obs}-i'_{obs}$) vs. i'_{obs} diagram. To determine the CMR we apply the 2σ–clipping fitting procedure to the cluster members: we obtain $V_{obs}-i'_{obs}$=1.910–0.018×i'_{obs}. Out of our photometric catalog, we consider as likely cluster members the objects lying within 0.1 mag of the CMR (see Fig. 11). We stress that the use of the above color-magnitude relation, fully based on our uncalibrated magnitudes, is valid and only valid within our own catalog. However, we need a (rough) idea of the magnitude correction to understand the deepness of our Subaru samples. To

this aim, we compare our uncalibrated magnitudes i'_{obs} and magnitudes i' of the common objects between Subaru catalog and the final INT catalog. The visual inspection of the $i'_{obs} - 0.1$ vs. i' plot, where 0.1 is the Galactic extinction correction, suggests us that $i'_{obs} \sim i' + 0.6$ mag.

Figure 12 shows the 2D-DEDICA results for the sample with $i' \leq 20.5$, comparable, for magnitude deepness, to the results from the INT sample with $r' \leq 21$. The $i' \leq 20.5$ sample confirms the presence of two density peaks in the galaxy distribution of A2254 and the presence of the external group (841 galaxies in the whole field). However, while the E-peak position is close to the INT E-peak, the W-peak is closer to the BCG position than the INT W-peak and both eastern and western structures are someway elongated in the N-S direction. These hints for a more complex structure are reinforced by the analysis of the $i' \leq 21.5$ Subaru sample (Fig. 12; 1257 galaxies in the whole field) where the W-structure is shown to be bimodal. Out of many peaks obtained through the 2D-DEDICA in the $i' \leq 21.5$ Subaru sample, Table 2 lists the results for the three densest peaks and the external peak for comparison. Since in this case $\chi^2_{threshold} \sim 40$, we cannot formally discard the possibility of noise fluctuations, but Fig. 2 of Ramella et al. (2007) suggests a small probability ($\sim 10\%$) of noise contamination when the χ^2 is about half of $\chi^2_{threshold}$. We do not show results for deeper Subaru samples since, working on galaxies in magnitudes bins, one realizes that the distribution of fainter galaxies is no longer centered around the cluster position, a likely sign of contamination by the background large scale structure.

The complex structure detected by the 2D–DEDICA method is confirmed by the Voronoi Tessellation and Percolation (VTP) technique (e.g. Ramella et al. 2001; Barrena et al. 2005). This technique is non-parametric and does not smooth the data. As a consequence, it identifies galaxy structures irrespective of their shapes. For our purposes we run VTP on the same sample of 1257 Subaru likely members with $i' < 21.5$. The result of the
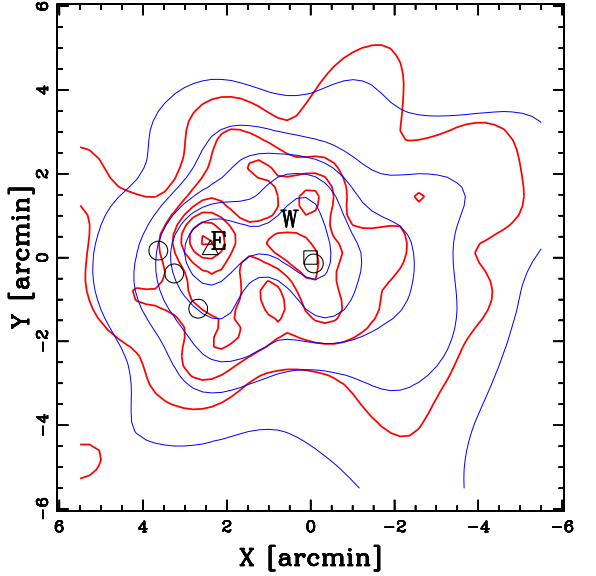
Fig. 12. Spatial distribution on the sky and relative isodensity contour map of Subaru photometric cluster members with $i' \leq 20.5$ and with $i' \leq 21.5$ (thin/blue and thick/red contours, respectively). Labels E and W indicate the peaks as detected by DEDICA in the INT sample (see Table 2). The BCG and other interesting galaxies are indicated as in Fig. 8.
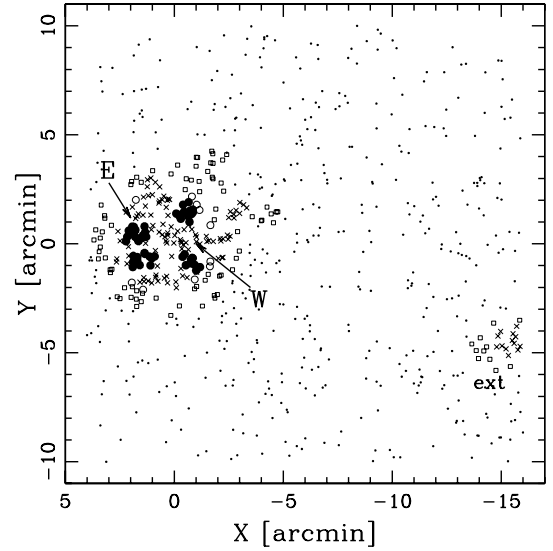
Fig. 13. Galaxies belonging to structures as detected by the Voronoi Tessellation and Percolation technique. The algorithm is run on the sample of likely members with $i' < 21.5$ extracted from the Subaru photometric catalog (see text). Open squares, open circles, crosses and solid circles indicate galaxies in structures at the 95%, 98%, 99% and 99.9% c. ls., respectively.

application of VTP is shown in Fig. 13. VTP is run four times adopting four detection thresholds: galaxies identified as belonging to structures at 95%, 98%, 99% and 99.9% c.ls. are shown as open squares, open circles, crosses and solid circles, respectively. VTP confirms the elongation of the eastern and western central structures in the N-S direction. In particular, the W-structure is clearly bimodal, and there are clues for a bimodality of the E-structure, too. Far from the cluster center, $17'$ WSW, VTP also confirms the existence of the ext-peak.

Interestingly, the ext–peak can be successfully identified with the cluster NSC J171627+193456 at $z_{phot} \sim 0.194$, discovered by Gal et al. (2003, based on the galaxy catalogs from the digitized Second Palomar Observatory Sky Survey). However, the absence of spectroscopic z in the region of this system does not allow to infer if it is a bound companion cluster in the outskirts of A2254 (projected at $\sim 3\ h_{70}^{-1}$ Mpc from the cluster center).

3.5. 3D analysis

3.5.1. Significance of 3D substructure

The existence of correlations between positions and velocities of cluster galaxies is a characteristic of true substructures. Here we use different approaches to analyze the structure of A2254 combining position and velocity information.

We find no evidence for a significant velocity gradient (see, e.g., den Hartog & Katgert 1996 and Girardi et al. 1996 for the details of the method).

In order to check for the presence of substructure, we combine velocity and position information by computing the Δ-statistics devised by Dressler & Schectman (1988, hereafter DS-test), which is recommended by Pinkney et al. (1996) as the most sensitive 3D test. For each galaxy, the deviation δ is defined as $\delta_i^2 = [(N_{nn}+1)/\sigma_V^2][(\overline{V}_l - \overline{V})^2 + (\sigma_{V,l} - \sigma_V)^2]$, where the subscript

"l" denotes the local quantities computed over the $N_{nn} = 10$ neighbors of the galaxy. Δ is the sum of the δ of the individual N galaxies and gives the cumulative deviation of the local kinematical parameters (mean velocity and velocity dispersion) from the global cluster parameters. The significance of Δ, i.e. of substructure, is checked by running 1000 Monte Carlo simulations, randomly shuffling the galaxy velocities. We find no significant presence of substructure.

Following Pinkney et al. (1996; see also Ferrari et al. 2003), we apply two more classical 3D tests: the ϵ-test (Bird, 1993) based on the projected mass estimator and the centroid shift or α-test (West & Bothun 1990). The details of these tests can be found in the above papers. We only point out that we consider ten as the number of the nearest neighbors for each galaxy and we use the above Monte Carlo simulations to compute the substructure significance. In both cases we do not find evidence for significant substructure.

We also consider two kinematical estimators alternative to the δ parameter of the DS-test, i.e. we consider separately the contributes of the local mean $\delta_V^2 = [(N_{nn}+1)/\sigma_V^2](\overline{V}_l - \overline{V})^2]$, and dispersion $\delta_s^2 = [(N_{nn}+1)/\sigma_V^2](\sigma_{V,l} - \sigma_V)^2]$ (see, e.g. Girardi et al. 1997, Ferrari et al. 2003). When considering the δ_s estimator, we find evidence for peculiar local velocity dispersion at the 97% c.l.. Figure 14 – lower panel – shows the distribution on the sky of all galaxies, each marked by a circle: the larger the circle, the larger the deviation $\delta_{s,i}$ of the local velocity dispersion from the global cluster value. The two largest deviations are obtained for the subgroups associated to two galaxies just south of the BCG for which $\sigma_{V,l} \sim 400$ km s^{-1}. Other deviations interest the eastern region characterized by large values of the velocity dispersion. To better investigate we repeat the DS-test increasing the number of neighbors. As for the δ_s indicator, we obtain large c.l. values for peculiarity up to a 99.99% c.l. in the $N_{nn} = 25$–50 range (see Fig. 15 – upper panel). This result suggests that
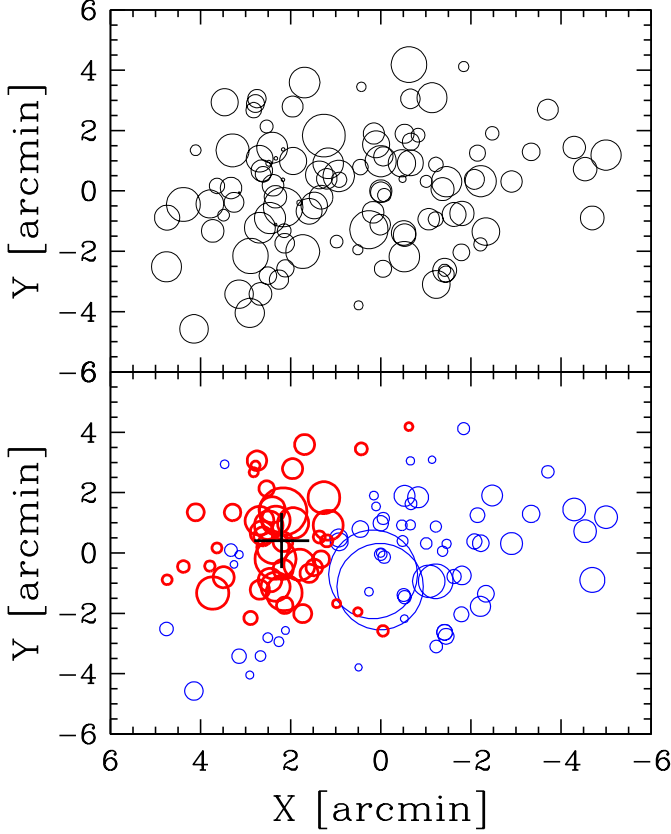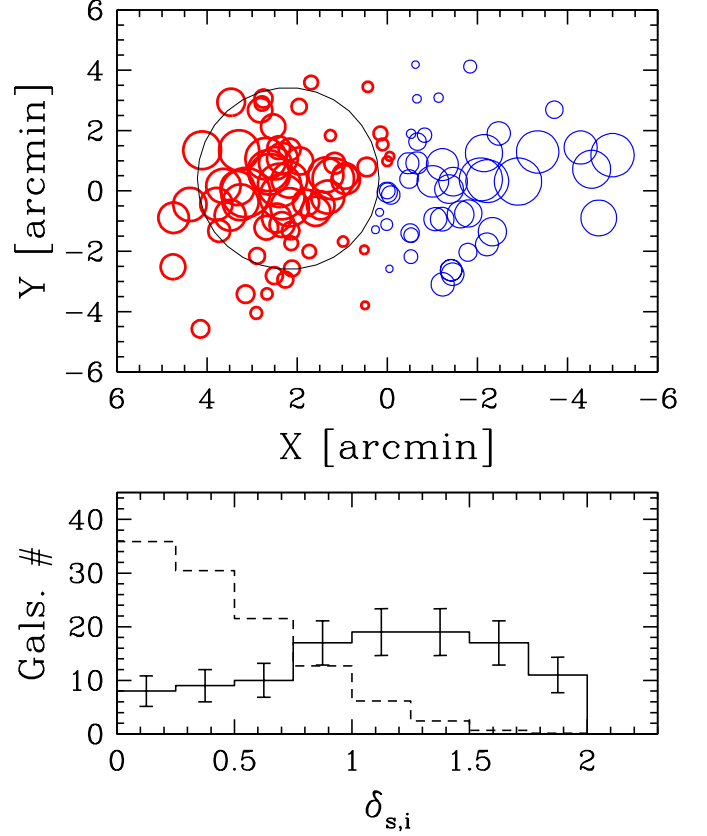
Fig. 14. Spatial distribution of the 110 cluster members, each marked by a circle. The plot is centered on the cluster center. *Upper panel:* the cluster velocity field: the larger the circle, the larger is the galaxy velocity. *Lower panel:* the result of the (modified) DS-test: the larger the circle, the larger is the deviation $\delta_{s,i}$ of the local velocity dispersion from the global velocity dispersion. Thin/blue and thick/red circles show where the local velocity dispersion is smaller or larger than the global value. The cross indicates the position of the E-peak as detected in the 2D analysis (INT sample).

Fig. 15. *Upper panel:* the same of Fig. 14 – lower panel but for the DS-test with a larger number of neighbors ($N_{nn} = 40$). The large, faint circle encloses the region within 1.5′ from the E-peak: galaxies inside defines the E1.5-sample. *Lower panel:* the distribution of $\delta_{s,i}$ deviations of the above DS-test. The solid line represents the observations, the dashed line the distribution for the galaxies of the 1000 simulated clusters, normalized to the observed number.

the peculiarity interests a large part of the cluster. To individuate how many galaxies are involved in the substructure, we resort to the technique developed by Biviano et al. (2002), who used the individual δ_i-values of the DS method. The comparison of the $\delta_{s,i}$-values of all 1000 Monte Carlo simulations and the observed values shows how many galaxies are involved in the structures with peculiar kinematics (Fig. 15 – lower panel).

3.5.2. Identifying subclusters in the eastern region

Comparing the two subsamples obtained by a rough division of A2254 (e.g., the eastern and the western subsamples with respect to the position of the BCG), we find that the eastern sample is characterized by a larger value of σ_V (see Table 3 and Fig. 16 – upper panel). The F-test confirms that the velocity dispersions of the two samples differ at the 99.4% c.l.; no difference is shown between the mean velocities according to the means-test (see,e.g., Press et al. 1992 for these tests).

Figure 15 – lower panel shows as the region with high $\sigma_{V,l}$ values is centered roughly around the E-peak as determined in

the 2D analysis. We select the galaxies within a circular region centered in the position of the E-peak. Using a radius of 1.5′, comparable to the distance between E- and W-peaks, we obtain a subsample of 27 galaxies, the E1.5-sample, characterized by a large value of $\sigma_V \sim 1700$ km s^{-1}. When applying the 1D-DEDICA method to this subsample we detect two significant peaks with 21 and 6 galaxies at $\sim 52\,500$ and $56\,300$ km s^{-1}, respectively (see E1.5LV and E1.5HV in Table 3). Figure 16 – lower panel – shows the results of the 1D-DEDICA method for the E1.5-sample, as well as for other two samples defined by a larger and a smaller radius (2′ and 1′). The choice of a large radius gives one-(asymmetric) peak in the galaxy density distribution in the velocity space, while a too small radius gives a list of non-significant peaks due to the poor statistics involved.

3.5.3. Identifying subclusters through the Htree method

We resort to the method devised by Serna & Gerbal (1996, hereafter Htree-method; see, e.g., Durret et al. 2010 for a recent application). This method uses a hierarchical clustering analysis to determine the relationship between galaxies according to their relative binding energies. The method assumes a constant value

Table 3. Kinematical properties of the whole system and galaxy subsystems.

Substructure results					3D KMM		
System	N_g	$<v>$ km s^{-1}	σ_V km s^{-1}	Interpretation	$N_{g,KMM}$	$<v>_{KMM}$ km s^{-1}	$\sigma_{v,KMM}$ km s^{-1}
Whole system	110	53128 ± 128	1340^{101}_{84}	–	–	–	–
Eastern system	58	53098 ± 208	1576^{168}_{104}	contaminated main	–	–	–
Western system	52	53186 ± 150	1073^{118}_{92}	uncontaminated main	–	–	–
E1.5HV	6	56310 ± 226	245^{86}_{180}	high vel. E – group	7	56414 ± 116	370^{291}_{181}
E1.5LV	21	52463 ± 341	1000^{220}_{102}	main	103	52968 ± 119	1180^{88}_{67}
HT2	7	56355 ± 244	232^{68}_{104}	high vel. E – group	8	56341 ± 115	469^{183}_{255}
HT1	96	52980 ± 108	1053^{59}_{66}	(substructured) main	–	–	–
HT12	8	51414 ± 159	421^{127}_{91}	low vel. W – main	35	51840 ± 100	889^{162}_{63}
HT11	42	53299 ± 188	739^{81}_{55}	principal main	67	53550 ± 153	939^{86}_{69}
DED1	3	56322 ± 139	197^a	high vel. E – group	4	56422 ± 109	167^{70}_{132}
DED2	9	54313 ± 213	579^{118}_{80}	NW – group	27	54246 ± 130	663^{98}_{68}
DED3	12	53151 ± 362	1171^{248}_{134}	E group	26	53385 ± 320	1591^{329}_{193}
DED4	30	53054 ± 177	950^{141}_{98}	SW group	46	52168 ± 114	763^{84}_{66}
DED5	4	51798 ± 293	448^{21}_{46}	low vel. SE – group	7	53238 ± 429	1000^{407}_{59}

[a] Standard velocity dispersion estimate.
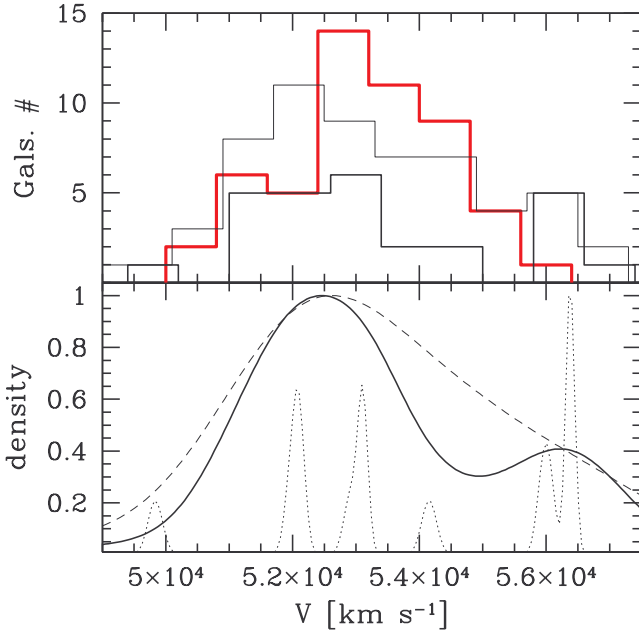
Fig. 16. *Upper panel:* velocity distributions of the galaxies in the western and eastern samples (thick/red and thin/black lines, respectively). The velocity distribution of a subsample of the eastern sample, i.e. the 27 galaxies within a radius of 1.5′ from the E-peak (E1.5-sample), is also shown (black thick line). *Lower panel:* the galaxy density distribution in the velocity space, as provided by the DEDICA adaptive-kernel reconstruction method for the E1.5-sample (solid line) and for two samples contained within a larger and a smaller radii, E2.0- and E1.0-samples (dashed and dotted lines, respectively). Unit on the y-axis is normalized to the density of the highest peak.

for the mass-to-light ratio of galaxies and Serna & Gerbal suggest a value comparable to that of clusters. Here we take a value of M/L_r=150 h_{70} $M_\odot/L_\odot$ as suggested by large statistical stud-

ies (e.g., Girardi et al. 2000; Popesso et al. 2005). The (gross) results are quite robust against the choice of the value of M/L_r.

Figure 17 shows the resulting dendogram, where the total energy appears horizontally. Galaxy pairs and subgroups of galaxies then appear with a lower total energy. Starting from the less deep part of the energy levels (right part of the dendogram) we find HT1, which we interpret as the main system, and the group HT2. HT2 is a high-velocity eastern group and contains all members of E1.5HV. HT1 is a "substructured" main system and is formed by HT11, which has the BCG in its potential well, and HT12, i.e. a few low velocity galaxies located in the western region (in particular, the BCG3). Note, however, that at the bottom of the binding energy of HT11 we find HT1111, which is not a core in the classical sense. In fact, HT1111 contains HT11111 and HT11112. HT11112 is formed by three galaxies close to the cluster center: the BCG and BCGc pair, and a small compact galaxy located between them. HT11111 is close to the E-peak and is formed by four galaxies, among which the BCG2 and BCG4.

3.5.4. Identifying subclusters through the 3D-DEDICA method

Finally, we apply the 3D-DEDICA method (Bardelli et al. 1998). Table 3 lists the five most significant ($\gtrsim$ 94% c.l.) groups (DED1–DED5) composed by at least three galaxies. The picture revealed by the 3D-DEDICA test is that of a very complex structure, with three and two subclusters in the eastern and western regions, respectively.

Figure 18 – left col. – shows the spatial distribution of the groups detected by above methods and Table 3 lists the kinematical properties: the number of assigned members, N_g (Col. 2); the mean velocity, $\langle v \rangle$ (Col. 3); the velocity dispersion with bootstrap errors, σ_V (Col. 4); a short comment summarizing our interpretation (Col. 5). Following properties refer to the corresponding KMM subclusters, see below (Cols. 6, 7, and 8).
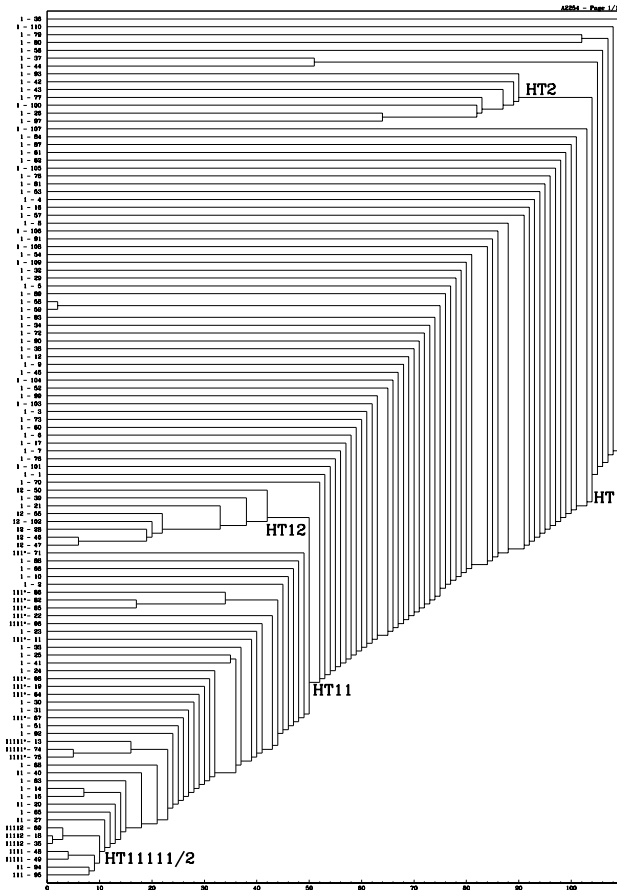
Fig. 17. Dendogram obtained through the Serna & Gerbal (1996) algorithm. The abscissa is the binding energy (here in arbitrary unit with the deepest negative energy levels on the left) while the catalog numbers of the various member galaxies are shown along the ordinate (IDm in Table 1).

Fig. 18. Spatial distribution on the sky of the galaxies of the subclusters detected through our 3D analysis and the cluster partitions obtained through the 3D-KMM method using them as seeds (*left and right panels*, respectively). In the *left panels* symbols refer to different groups. The different colors refer to different mean velocities according to the legend at the top of the figure. In the *right panels* symbols indicate subclusters found using as seeds the respective groups on the left and colors refer again to the velocity according to the above legend.

3.5.5. 3D-KMM method

We use the above results to apply the full 3D-KMM method, which, starting from the above seeds, allow us to assign all galaxies to subclusters.

Using E1.5LV and E1.5HV as seeds for a initial two-group partition, we find that a partition of 103 and 7 galaxies is a significantly more accurate description of the 3D galaxy distribution than a single 3D Gaussian (at the 99.7% c.l.). We note that the KMM-E1.5LV subcluster. i.e. the main system, has a significant weighted gap in its velocity distribution (as in the whole sample, see Sect. 3.3) but does not show any trace of peculiar kinematics according to the DS-test. Using HT1, HT2, and HT1111 as initial seeds, the 3D-KMM converges to a three-group partition significant at the 97.5% c.l.. Finally, using DED1–DED5 groups as initial seeds we find the 3D-KMM test converges to a five-group partition significant at the 99.9% c.l..

Figure 18 – right col. – shows the spatial distribution of the obtained partitions.

4. X-ray morphological and spectral analysis

4.1. Observation and data reduction

A2254 was observed by *XMM-Newton* on August 26, 2009. The data were reduced with SAS v10.0 using the tasks *emchain* and *epchain*. We only considered event patterns 0–12 for MOS and 0 for pn, and the data were cleaned using the standard procedures for bright pixels and hot columns removal (by applying the expression FLAG == 0) and pn out-of-time correction. The energy scale of the pn over the whole spectral bandpass was further improved with the task *epreject*. Periods of high background event counts due to soft protons were filtered using a threshold cut method: we performed a Gaussian fit to the peak of the histogram of the light curve and excluded the time bins where the count rate lies more than 3σ away from the mean. The light curves were extracted from regions of least source contamination (excising the bright object core in the central 8′ and the point source list from the SOC pipeline, after visual inspection) in two different energy bands: a hard band, 10–12 keV for MOS and 10–13 keV for pn (using 100s bins), and a wider band, 0.5–10 keV (using 10s bins), as a safety check for possible flares with soft spectra. The flaring periods thus determined were further checked by visual inspection of the light curves, resulting in net exposures of 57.0 ks, 56.8 ks, and 45.1 ks for the MOS1, MOS2, and pn detectors, respectively. Point sources were detected using the task *ewavelet* in the energy band 0.5–10

keV and checked by eye on images generated for each detector. Detected point sources from all detectors were merged, and the events in the corresponding regions removed from the event list using circular regions of 25″ radius centered at the source position. The area lost by point source exclusion, CCD gaps, and bad pixels was calculated using a mask image. Redistribution matrix files (RMFs) and ancillary response files (ARFs) were generated with the SAS tasks *rmfgen* and *arfgen*, the latter in extended source mode. Appropriate flux-weighting was performed for RMFs, and for ARFs using exposure-corrected images of the source as detector maps (with pixel size of 1′, the minimum scale modeled by *arfgen*) to sample the variation in emission, following the prescription of Saxton & Siddiqui (2002). For the background subtraction, we adopted a complete modeling of the various background components as described in detail in Gastaldello et al. (2007). We accurately modeled the actual sky background using a region free of cluster emission at $r > 9′$, where the surface brightness profile in the 0.7–1.2 keV reaches the background level. The spectra of the out-of-field-of-view events of CCD 4 and 5 of MOS1 showed an anomalously high flux in the soft band (see Kuntz & Snowden 2008) so they were excluded from our surface brightness and spectral analysis.

4.2. X-ray image and surface brightness analysis

For each MOS detector, we create images in the 0.5–2 keV band and exposure maps at the monochromatic energy of 1 keV and then combine the images into a single exposure-corrected image, smoothed on a scale of 12″, as shown in Fig.19. We process the image to remove the point sources using the CIAO tool *dmfilth*, which replaces photons in the vicinity of each point source with a locally estimated background. We consider only the regions exposed by more than 65% of the maximum exposure (see Fig. 20) in order to perform the X-ray morphology analysis. We adopt quantitative measures by applying the power ratios technique (Buote & Tsai 1996), the centroid shifts (Mohr et al. 1993) and the concentration parameter (Santos et al. 2008).

Power ratios derive from multipole expansions of the two-dimensional projected gravitational potential and they can be applied directly on X-ray images since under normal circumstances the X-ray emissivity can be used as a proxy for the gravitational potential. Power ratios are computed within a fixed circular aperture and they can be computed on the centroid of the cluster or on the X-ray peak. In the former case P_1/P_0 is null, P_2/P_0 gives information on the ellipticity of the cluster, P_3/P_0 is related to a bimodal structure and P_4/P_0 is sensitive on small scale substructure. In the latter case P_1^{pk}/P_0^{pk} is non null if the cluster does not exhibit reflection symmetry about two orthogonal axes originating on the peak of the emission and it is essentially a circularly average centroid shift. We calculate the power ratios within an aperture of 500 kpc, given the high signal-to-noise within this radius and for comparison with previous work.

Centroid shifts indicate that the center of mass of the X-ray emitting gas varies with radius. Centroid shifts and power ratios are both capable of identifying highly disturbed systems or systems with significant, well defined substructures (Poole et al. 2006). However the centroid shifts parameter, w, is more sensitive to subtler disturbances. Following the method of O'Hara et al. (2006, see also Poole et al. 2006), the centroid shift is computed in a series of circular apertures centered on the cluster X-ray peak. The radius of the apertures is decreased in steps of 5% from 500 kpc to 25 kpc.
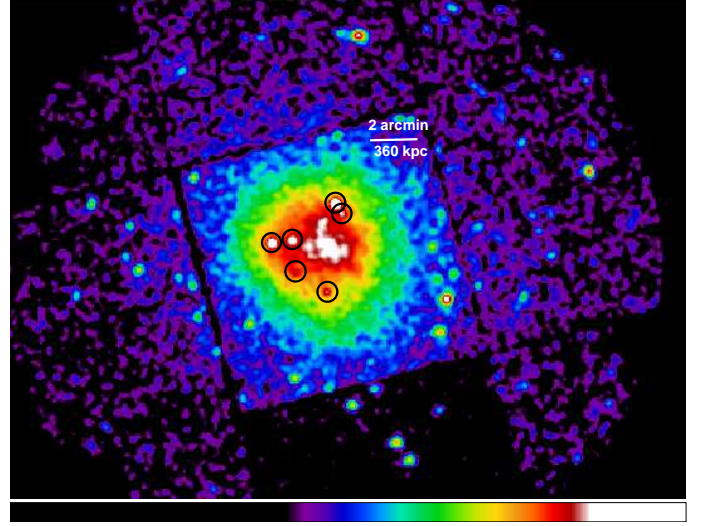
Fig. 19. Mosaic of the MOS1 and MOS2 images in the 0.5–2 keV energy band smoothed on a 12″scale. The image was divided by the summed exposure maps to correct for exposure variations. The detected point sources within the central regions of the cluster discussed in the text are highlighted by black circles.
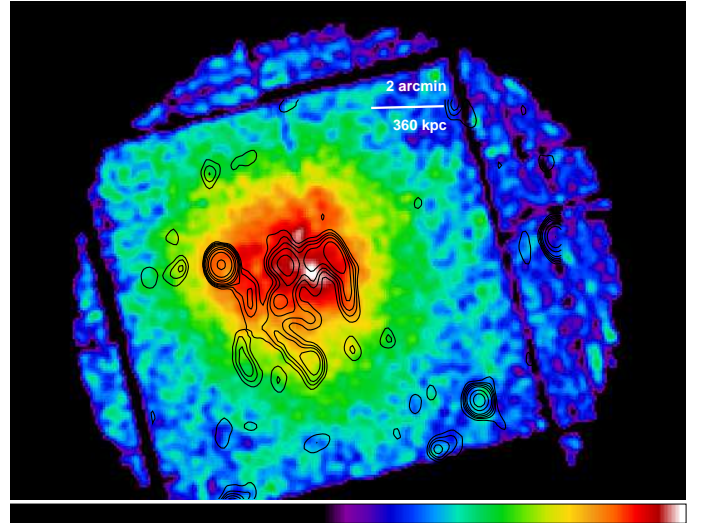

Fig. 20. X-ray image of the diffuse emission of the A2254 cluster where point sources were removed and replaced by a local estimate of the surrounding emission and only regions exposed by more than 65% of the maximum exposure is considered. The contour levels of the radio VLA image (Govoni et al. 2001b) are superimposed, too

The concentration parameter, c, is defined as the ratio of the peak (calculated within 100 kpc) over the ambient surface brightness (calculated within 500 kpc). We apply these techniques to the image reported in Fig. 20 and the results are reported in Table 4.

Following Ettori et al. (2010) we extract the surface brightness profile in the energy band 0.7–1.2 keV, in order to keep the background as low as possible with respect to the source. For this reason, we avoid the intense fluorescent instrumental lines of Al (~ 1.5 keV) and Si (~ 1.8 keV). We account for the X-ray background by including a constant background component. The data are grouped to have at least 20 counts per bin in order

Table 4. Results of the morphological analysis of the X-ray image of A2254 using power ratios, centroid shifts and concentration.

P_1^{pk}/P_0^{pk} $(\times 10^{-4})$	P_2/P_0 $(\times 10^{-7})$	P_3/P_0 $(\times 10^{-7})$	P_4/P_0 $(\times 10^{-8})$	w $(500\ h_{70}^{-1}\ \text{kpc})$	c
1.84 ± 0.47	4.25 ± 1.26	2.51 ± 0.82	1.29 ± 1.12	0.037 ± 0.001	0.08
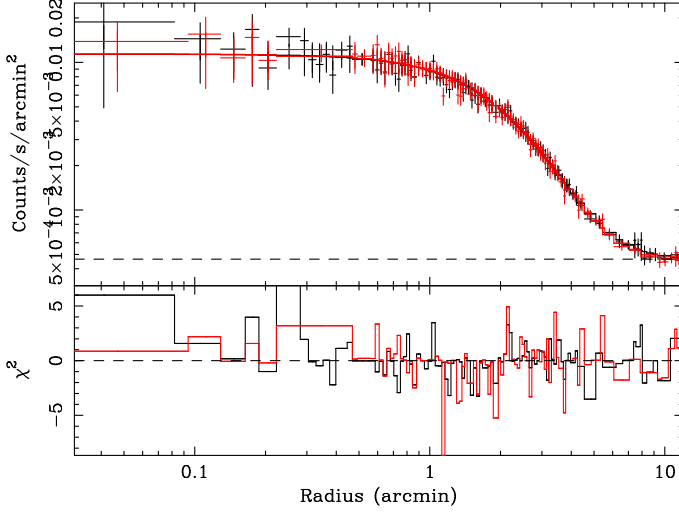
Fig. 21. Surface brightness profile of the X-ray emission of A2254. Data from MOS1 and MOS2 are plotted in black and red, respectively. The best fit β-model and ratio of data over the model are also shown. The background level is shown as the black dashed line in the lower panel.

to apply the χ^2 statistics. The fitted model is convolved with the *XMM-Newton* PSF. The joint best-fit β-model has a core radius of $r_c = (507 \pm 36)\ h_{70}^{-1}$ kpc $(169'' \pm 12'')$ and $\beta = 0.95 \pm 0.06$ for a $\chi^2/\text{d.o.f.} = 215/179$ (see Fig.21).

4.3. Spectral analysis

We extract spectra for each detector in 5 concentric circular annuli located at the the peak of the X-ray emission with bounding radii $0'$–$0.5'$, $0.5'$–$1.5'$, $1.5'$–$2.5'$, $2.5'$–$3.5'$, $3.5'$–$4.5'$. The spectra from the three detectors are re-binned to ensure a signal-to-noise ratio of at least 3 and a minimum 20 counts per bin (necessary for the validity of the χ^2 minimization method). We fit the spectra with an APEC thermal plasma modified by Galactic absorption fixed at 4.7×10^{20} cm^{-2} (Kalberla et al. 2005) to each annulus. A correction file derived from the background modelling is used in XSPEC as in Gastaldello et al. (2007). The free parameters are temperature, normalization (proportional to emission measure), and the metallicity, with the solar abundance units of Grevesse & Sauval (1998). The spectra are adequately fitted by the model, with reduced χ^2 ranging from 1.06 in the inner annulus to 1.5 in the outermost annulus. The azimuthally averaged, projected temperature and abundance profile thus obtained are shown in Fig. 22. The temperature profile is rather flat and in particular there is no evidence of a decrease in the core, as found in non-cool core clusters. We calculate the mean temperature of the cluster as the temperature
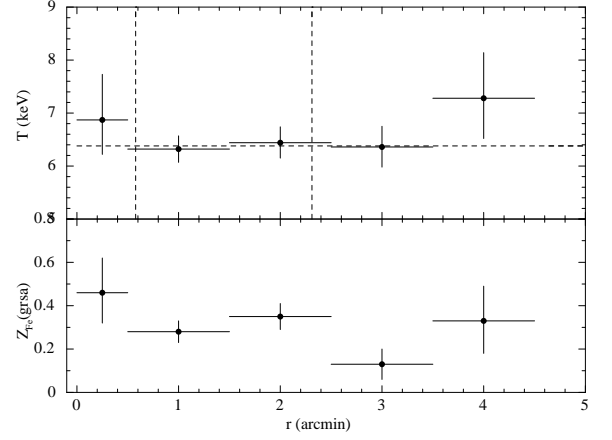

Fig. 22. Profiles of the azimuthally averaged, projected temperature and metal abundances of A2254. The error bars are at the 68% c.l.. The horizontal line shows the value of kT_{OUT}, i.e. the value of kT estimated within the $0.05R_{180} < r < 0.2R_{180}$ region, the two radii being indicated by the two vertical lines.

obtained with a spectral fit in the region $0.05R_{180} < r < 0.2R_{180}$, where $R_{180} = 1780(kT/5\text{keV})^{1/2} h(z)^{-1}\ h_{70}^{-1}$ kpc (Arnaud et al. 2005, with $h(z) = (\Omega_M(1+z)^3 + \Omega_\Lambda)^{1/2})$ using an iterative procedure to calculate kT and R_{180} (Rossetti & Molendi 2010). We find $kT = 6.38 \pm 0.25$ keV and $R_{180} = 2.08\ h_{70}^{-1}$ Mpc. The value of kT thus estimated within the $0.05R_{180} < r < 0.2R_{180}$ region, hereafter kT_{OUT}, is a good proxy for the global temperature (see Fig. 4 of Leccardi & Molendi 2008 where kT_M is the global temperature). In particular as for A2254, Figure 22 shows as the measure of kT has already large uncertainties around $0.4R_{180}$.

To characterize temperature and emission measure gradients, we compare the central to a global value of the pseudo-entropy measure. Following Leccardi et al. (2010), we compute the pseudo-entropy ratio $\mathcal{E} = (kT_{IN}/kT_{OUT}) \times (EM_{IN}/EM_{OUT})^{-1/3}$, where kT and EM are the X-ray temperature and emission measure, and IN and OUT define the region within the radius $\approx 0.05\ R_{180}$ and the region within the the annulus with bounding radii 0.05-$0.20\ R_{180}$, respectively. Note that Rossetti & Molendi (2010) proved that the pseudo-entropy ratio used in their study is a good proxy of the deprojected quantity and Rossetti et al. (2011, their Fig. 3) found a good correlation between the pseudo-entropy ratio and, for example, the central entropy defined in Cavagnolo et al. (2009). We measure $\mathcal{E} = 0.833 \pm 0.097$ which places A2254 among clusters with high entropy core (see also Sect. 5.1).

We also prepare a two dimensional map of X-ray temperature, starting from the EPIC images. We use a modified version of the adaptive binning and broad band fitting technique described in Rossetti et al. (2007), where we substitute the Cappellari & Copin (2003) adaptive binning algorithm with the weighted Voronoi tessellation by Diehl & Statler (2006, see Rossetti & Molendi 2010). The temperature map is shown in Fig. 23. The formal errors given in output from the procedure are of the order of 15–20% but the measures at the map periphery, more affected by the background, should be considered with more caution.
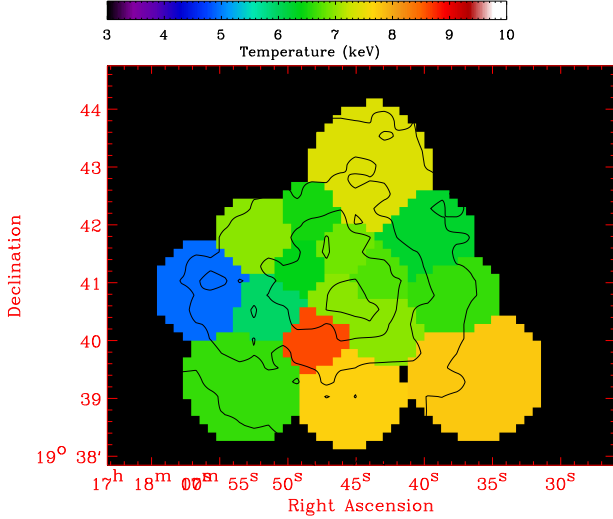
Fig. 23. Temperature map (keV) with, superimposed, the contour levels of the XMM image. Coordinates are right ascension and declination (J2000).

5. Discussion and conclusions

5.1. Cluster structure

The high values of the velocity dispersion $\sigma_V = 1340^{+101}_{-84}$ km s^{-1} and X-ray temperature $kT = (6.38 \pm 0.25)$ keV are comparable to the values found for hot, massive clusters (Mushotzky & Scharf 1997; Girardi & Mezzetti 2001). However, our estimates of σ_V and T_X are 3σ-inconsistent each other under the assumption of the equipartition of energy density between ICM and galaxies. In fact, we obtain $\beta_{spec} = 1.71^{+0.26}_{-0.21}$ to be compared with $\beta_{spec} = 1$, where $\beta_{spec} = \sigma_v^2/(kT/\mu m_p)$ with $\mu = 0.58$ the mean molecular weight and m_p the proton mass (see also Fig. 6). Evidence that A2254 is well far from the dynamical equilibrium comes from both optical and X-ray analyses as discussed in the following.

From the optical point of view, we find a strong evidence of bimodality from our 2D analysis of the photometric sample with the E and W-peaks far by $\sim$0.4–0.5 h_{70}^{-1} Mpc. The (modified) DS-test also shows evidence of substructure at a very high level (at the 99.99% c.l.). Our 3D analysis of the region of the 2D E-peak, detects a high velocity subcluster which explains the high velocity dispersion in that region and the strong increase of velocity dispersion profile at $\sim$ 0.4–0.5 h_{70}^{-1} Mpc from the cluster center (see Fig. 6).

However, a simple bimodal structure is not completely satisfactory when looking at the whole observational scenario. In fact, the W-peak is not well centered onto the BCG and both E- and W-peaks seem to have, at their turn, a bimodal or a N-S elongated structure (see Figs. 12 and 13). The E-subcluster recov-

ered through the 3D analysis is a minor structure and contains no dominant galaxy: it seems improbable that it causes the presence of the 2D E-peak which is almost as rich as the W-peak (see Table 2). Indeed, more refined 3D analyses (e.g., the H-tree and the 3D-DEDICA methods) show evidence for a more complex structure. In particular, the H-tree method detects a low-velocity eastern subcluster which can explain even better the important 2D E-peak and the strong increase of the velocity dispersion profile at $\sim$ 0.4–0.5 h_{70}^{-1} Mpc from the cluster center. The low-velocity eastern subcluster might also explain the results of the weighted gap analysis (see Fig. 7). The 3D-DEDICA analysis reveals five subclusters, two of which in the western region: they might explain the presence of a bimodal 2D W-peak.

We stress that our identification of subclusters are always confirmed by the 3D-KMM analysis. In principle, one might use the significance (as computed according to the likelihood ratio test statistics), to select the best cluster partition (e.g., Bird 1994). However, we note that in A2254, the high velocity E-group is the only subcluster well contained in the region sampled by our redshift data, while other subclusters have a large size and/or are at the boundary of this region. Thus, although the use of the 3D-KMM approach seems useful to perform a homogeneous check of the subclusters detected using other disparate methods, we do not rely on the 3D-KMM results to fix the best partition of subclusters and the relevant kinematical properties. To obtain more stringent conclusions on the structure of A2254 we stress the need of more galaxy redshifts and a more extended sampled region.

As for the X-ray data, all the methods of the morphological analysis provide evidence of a dinamically disturbed cluster: i) the power ratio analysis, with its value of $P_1^{pk}/P_0^{pk} = 1.85 \pm 0.47$ together with the radio power at 1.4 GHz of $P_{1.4GHz} = 2.9 \times 10^{24}\ h_{70}^{-2}$ W Hz^{-1} (Govoni et al. 2001b) places A2554 in the region of well known radio halo mergers, such as Abell 2256 and Abell 665, on the $P_1/P_0 - P_{1.4GHz}$ relation of Buote (2001; see their Fig. 1-left, where $P_{1.4GHz} = 2.1 \times 10^{24}$ W Hz^{-1} in their cosmology); ii) the combination of the three morphology indicators (as done by Cassano et al. 2010b) in the (w, c), $(P_3/P_0, c)$, and $(P_3/P_0, c)$ planes designates A2254 as a morphologically disturbed cluster among the other clusters with radio halo in the sample of that paper. In fact, A2254 shows well higher values of w and P_3/P_0 and a lower value of c with respect to the median discriminating values between disturbed and relaxed systems, i.e. $w = 0.012 \times 500\ h_{70}^{-1}$ kpc, $c = 0.2$, and $P_3/P_0 = 1.2 \times 10^{-7}$. iii) The value of $w = (0.037 \pm 0.001) \times 500\ h_{70}^{-1}$ kpc gives a significant indication of a non relaxed system. It is an intermediate value among those measured for 45 ROSAT-observed clusters by O'Hara et al. (2006). According to the simulations by Poole et al. (2006, their Fig. 11) this value of w is typical of ongoing cluster mergers.

The active dynamical state of A2254 is also confirmed from the thermodinamic point of view, given the absence of a temperature drop in the core and the classification of A2254 as an high entropy core according to Leccardi et al. (2010) who fixed the separation value between medium and high entropy core cluster at $\mathcal{E}=0.64$ ($\mathcal{E}= 0.833 \pm 0.097$ in A2254). In fact, observations seem to favor cool core destruction through cluster mergers (Allen et al. 2001; Sanderson et al. 2006) and the vast majority of merging systems hosts high entropy cores according to Leccardi et al. (2010), who analyzed 59 clusters spanning a large range of dynamical states. The temperature map, limited by the quality of the data to the inner regions, reveal a hot core with no significant temperature variations, consistent with an on-going merger.

5.2. Optical – X-ray – radio data comparison

At large scale, when comparing data from different wavelengths, the main feature is the correlation between the elongation of the optical structure, with the two galaxy clumps far by ~0.5 h_{70}^{-1} Mpc along the E-W direction, and the E-W elongation of the X–ray emission isophotes (see Fig. 1). The elongation of X-ray isophotes in the merging direction is expected from simulations (e.g., Roettiger et al. 1996). At small scale, we note that the X-ray emission is peaked at the BCG galaxy. Instead, the E-peak does not coincide with a secondary X-ray peak. This discrepancy between the distributions of the ICM (collisional) and galaxies (non collisional component) is a strong point in favor of an on-going cluster merger.

Our interpretation of the above correlations or no-correlations in the context of A2254 scenario is the following. The almost "triangular" shape of external X-ray isophotes indicates that the high velocity E-group has just passed through the main system going from west to east, as suggested by the comparison of Fig. 20 with, e.g., the second or third panels – or maybe the fourth panel considering a possible projection effect – in Figs. 4 and 5 of Poole et al. (2006 – top line, where the subcluster comes from the left). This scenario agrees with the fact that we observe the high-velocity E-group peak of galaxies being more advanced in the merging direction while the ICM component is slowed down and left behind (see e.g., the bullet cluster by Markevitch et al. 2002). At difference with the bullet cluster, A2254 does not reveals a secondary X-ray peak: this might be due to a more advanced phase of the merger or, in agreement with our mass estimates (see below), with the fact that the subcluster is much smaller and thus completely stripped by its gas content.

However, a simple bimodal merger is not completely satisfactory. In fact, the X-ray emission in the internal cluster region, i.e. in the region of the W-peak, also reveals an elongation toward the North, perpendicular to the merging direction (see Figs. 19 and 20). This could be connected to a particular phase of the the E-W merger resembling the high emission structure perpendicular to the merger at the time of the apocenter (but not in its symmetric aspect, see Fig. 4 of Poole et al. 2006). Alternatively, it could be connected with another accretion phenomenon – along the N-S direction. In fact, optical 2D analyses of deep Subaru data (see Figs. 12 and Figs. 13) reveal a N-S double structure in the cluster center: one enclosing the BCG and one slightly at north. The 3D DEDICA analysis finds a northern and a southern galaxy clumps in the western part of the cluster, too.

As for its radio morphology, A2254 is the most irregular in its radio morphology in the sample of Govoni et al. (2001b). The halo is not centered on the region of the maximum X-ray emission (see its upside-down "U" shape in Figs. 1 and 20), resembling in some respects the behavior of radio relics. As for the comparison between radio and other data, the main feature is its bad correlation, already at large scales, with X-ray emission, and with the merging direction suggested by the two optical subclusters. In fact, here the halo does not permeate the cluster volume in a similar way to the X-ray emitting gas of the intracluster medium (see Fig. 1) as generally shown in other clusters not only by their large scale morphology but also by the point-to-point correlation between radio and X-ray brightness (see the case of the four clusters analyzed by Govoni et al. 2001a). Moreover, halos are round or elongated in the direction of the merger (the bullet cluster by Markevitch et al. 2002; Abell 520 by Girardi et al. 2008; Abell 754 by Macario et al. 2011): this is not the case of the A2254 halo.

Our interpretation is that the peculiar radio morphology of A2254 is likely due to the very complex substructure of A2254. In particular, the two N-S elongated branches of the radio emission might be connected with the minor N-S mergers suggested by our optical analysis. However, note that, although the "U" shape morphology of the radio halo (see Fig. 1) recalls the "H' shape of the contours in the galaxy distribution in Fig. 12, the two features are shifted one respect to the other along the E-W direction.

Finally, we stress the absence of a connection between bright galaxies and subclusters, while this is often found in complex systems in 2D (e.g., Geller & Beers 1982), in 3D (e.g., Abell 520, Girardi et al. 2008), and also when a subcluster is partially destroyed (see the beautiful example of the tidal debris in A2744 by Owers et al. 2011). In A2254, neither the high-velocity E-peak, the best detected through our optical analysis, hosts a bright, dominant galaxy. The feature which is worthy of mention, in spite of the poor statistics, is that BCG2, BCG3, and BCG4 are all located on the eastern side of the cluster, more external than respect to the E-subcluster. However, their optical spectra do not show features – e.g. emission lines or a strong H_δ absorption – typical of a possible starburst or poststarburst activity triggered by the shocked gas during a cluster-cluster merger (Bekki et al. 2010), thus there is no clear connection with the ongoing merger.

5.3. A simple model for mass and merging scenario

Following the above discussion, A2254 can be described in first approximation by a main system and an eastern high velocity group. Looking at Table 3 we can estimate σ_V ~ 1000–1200 km s^{-1} and σ_V = 200–500 km s^{-1} for the main and the E-group, respectively.

Making the usual assumptions for the main system and the subcluster (cluster sphericity, dynamical equilibrium, coincidence of the galaxy and mass distributions), we can compute virial global quantities. We follow the prescriptions of Girardi & Mezzetti (2001, see also Girardi et al. 1998) and compute R_{vir} – an estimate for R_{200} – and the mass contained within this radius. In particular, we assume for the radius of the quasi-virialized region $R_{vir} = 0.17 \times \sigma_v/H(z) \ h_{70}^{-1}$ Mpc(see Eq. 1 of Girardi & Mezzetti 2001 with the scaling of $H(z)$ of Eq. 8 of Carlberg et al. 1997 for R_{200}). For the mass we use $M = M_V - SPT = 3\pi/2 \cdot \sigma_V^2 R_{PV}/G -$ SPT (Eq. 3 of Girardi & Mezzetti 2001), with R_{PV} computed using the full procedure (see also Eq. 13 of Girardi et al. 1998, with $A = R_{vir}$ for a close approximation) and the surface pressure term correction $SPT = 0.2 \times M_V$. In practice, both R_{vir} and M can be computed on the basis of the estimated velocity dispersion with the usual scaling-laws $R_{vir} \propto \sigma_V$ and $M(< R_{vir}) \propto \sigma_V^3$.

We compute $M(< R_{vir} = 2.2–2.7 \ h_{70}^{-1}Mpc) = 1.5–2.5 \times 10^{15} \ h_{70}^{-1} \ M_\odot$ and $M(< R_{vir} = 0.4–1.2 \ h_{70}^{-1}Mpc) = 0.1–1.8 \times 10^{14} \ h_{70}^{-1} \ M_\odot$ for the main and the E-group respectively, leading to a small mass ratio for the merger (< (1 : 10)). We compute a mass $M_{sys}(< R = 2.2–2.7 \ h_{70}^{-1}Mpc) = 1.5–2.9 \times 10^{15} \ h_{70}^{-1} \ M_\odot$ for the whole system, where we assume that $M \propto R$ to roughly extrapolate the mass of the E-group. According to the virial scaling laws, the above mass range leads to σ_V ~ (1000–1250) km s^{-1} for the virial velocity dispersion, thus making acceptable the $\beta_{spec} = 1$ model.

For comparison, we would obtain $M_{sys,1}(< R_{vir,1} = 3.0 \ h_{70}^{-1}Mpc) = (3.5 \pm 1.0) \times 10^{15} \ h_{70}^{-1} \ M_\odot$ when assuming A2254 as a dynamically relaxed cluster and $M_{sys,5}$ ~ 4

$\times 10^{15} \, h_{70}^{-1} \, M_\odot$ when assuming A2254 is the very complex cluster formed by the five DEDICA subclusters.

We use X-ray data to compute an alternative mass estimate. Given the no significant departures from the isothermality of the temperature profile out to $\sim 0.9 \, h_{70}^{-1}$ Mpc (see Fig. 22), we derive a mass estimate using the isothermal beta model where the total mass profile can be expressed by a simple analytical formula (e.g., eq. 6 of Henry et al. 1993 with $\gamma = 1$). Using the value of kT_{OUT} and the fitted parameters of the β model to the surface brightness (Sect. 4.1), we obtain a mass $M_X(< R = 0.9 \, h_{70}^{-1} \text{Mpc}) = 0.48 \times 10^{15} \, h_{70}^{-1} \, M_\odot$ with nominal errors less than the 5%. We rescale the optical mass M_{sys} to $R = 0.9 \, h_{70}^{-1}$ Mpc assuming that the system is described by a King-like mass distribution with a very small core radius (Girardi et al. 1998) or, alternatively, a NFW profile where the mass-dependent concentration parameter c is taken from Navarro et al. (1997) and rescaled by the factor $1 + z$ (Bullock et al. 2001; Dolag et al. 2004), here $c \sim 4$. We obtain $M_{sys}(< R = 0.9 \, h_{70}^{-1} \text{Mpc}) = (0.6$–$1.0) \times 10^{15} \, h_{70}^{-1} \, M_\odot$ to be compared with the above $M_X(< R = 0.9 \, h_{70}^{-1} \text{Mpc}) \sim 0.5 \times 10^{15} \, h_{70}^{-1} \, M_\odot$. Thus, when opportunely correcting the optical mass for the presence of substructure, we do not find a large discrepancy between optical and X-ray mass estimates in agreement with that $\beta_{spec} = 1$ is acceptable (see above).

Taking the above face on values, one might estimate that the non-thermal pressure in A2254 ranges from a value of 10% to 100% of the gas thermal pressure. However, note that the above comparison of the two mass estimates should be considered at best a tentative since the multiclump structure of the cluster should be better known. Indeed, previous efforts on making a comparison to put a limit on non-thermal pressure have targeted systems which can be assumed in equilibrium at least in the non-collisional component (e.g., a sample of elliptical galaxies by Churazov et al. 2010).

We can use our results to examine A2254 with respect to the observed scaling relations among $P_{1.4GHz}$, the halo radio power, and M_H, the total cluster mass contained within the size of the radio halo, R_H (Cassano et al. 2007). We rescale the mass M_{sys} to $R_H = 0.4 \, h_{70}^{-1}$ Mpc (Cassano et al. 2007) and obtain $M_{sys}(< R_H = 0.4 \, h_{70}^{-1} \text{Mpc}) = (0.2$–$0.5) \times 10^{15} \, h_{70}^{-1} \, M_\odot$. Thus A2254 is well in agreement with the relation fitted for other clusters with radio halos (see Fig. 9 of Cassano et al. 2007).

We also attempt to analyze the cluster merger between the main system and the high velocity E-group. Even if the substructure of A2254 is more complex, the elongation of the X-ray surface brightness suggests that this merger is the most recent one. We apply the two-body model (Beers et al. 1982; Thompson 1982) following the methodology outlined for other DARC clusters, e.g., Abell 520 (Girardi et al. 2008) and Abell 2345 (Boschin et al. 2010). The values of the relevant parameters for the two-subclusters system are: the above $M_{sys} = 1.5$–$2.9 \times 10^{15} \, h_{70}^{-1} \, M_\odot$, the relative LOS velocity in the rest-frame, $\Delta V_{rf,LOS} \sim 3000$ km s^{-1}, and the projected linear distance between the two clumps, $D \sim 0.5 \, h_{70}^{-1}$ Mpc, taken as the distance between the BCG and the 2D E-peak. The comparison between the observed shape of the X-ray surface brightness isophotes and the simulated ones (Poole et al. 2006) suggests we can assume to see the merger after the core crossing and not too much after the apocenter. For comparison with other clusters hosting radio halos, the time t elapsed from the core crossing is generally few fractions of Gyr (e.g., Markevitch et al. 2002; Girardi et al. 2008). Figure 24 compares the bimodal-model solutions as a function of α, where α is the projection angle between the plane of the sky and the line connecting the centers of the two
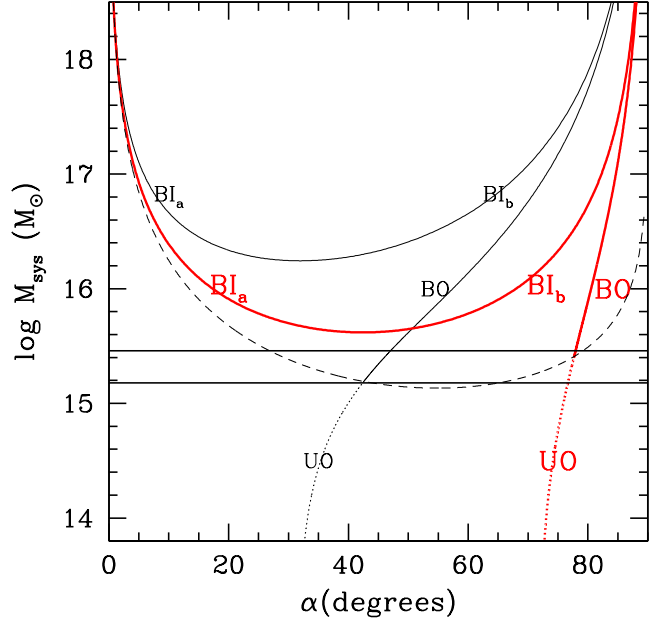
Fig. 24. System mass vs. projection angle for bound and unbound solutions (thick solid and thick dashed curves, respectively) of the two–body model applied to the high velocity E-group and the main cluster. Thin/black and thick/red lines refer to $t = 0.1$ Gyr and $t = 0.5$ Gyr, respectively. Labels BI$_a$ and BI$_b$ indicate the bound and incoming, i.e., collapsing solutions (solid curve). Label BO and UO indicate the bound outgoing, i.e., expanding solutions and unbound outgoing solutions (solid curve going on in the dotted curve, respectively). The horizontal lines give the range of observational values of the mass system. The thin dashed curve separates bound and unbound regions according to the Newtonian criterion (above and below the thin dashed curve, respectively).

clumps, with the observed mass of the system M_{sys}. We consider two different cases ($t = 0.1$ Gyr and $t = 0.5$ Gyr). In both cases we find a bound outgoing solution (BO) with $\alpha \sim 45°$, and $\alpha \sim 75°$, respectively. These intermediate angles are someway in agreement with the fact that we can detect the E-peak in the 3D analysis, which is the most efficient for intermediate angles (Pinkney et al. 1996). These angles lead to a deprojected relative velocity $\Delta V_{rf} \sim 3100$–4200 km s^{-1} of the subcluster with respect to the main system, comparable to that of the bullet cluster (Markevitch et al. 2002) or of Abell 2744 (Boschin et al. 2006).

In conclusion, A2254, for its large mass and unrelaxed dynamical status, fits well among typical clusters with radio halos described in the literature. Present data agree with the scenario of a recent merger with a minor subcluster, but we have evidence for a more complex dynamical history which should be better investigated to explain the peculiar radio morphology.

References

Abell, G. O., Corwin, H. G. Jr., & Olowin, R. P. 1989, ApJS, 70, 1

Allen, S. W., Ettori, S., & Fabian, A. C. 2001, MNRAS, 324, 877

Arnaud, M., Pointecouteau, E., Pratt, G. W. 2005, A&A, 441, 893

Ashman, K. M., Bird, C. M., & Zepf, S. E. 1994, AJ, 108, 2348

Bardelli, S., Pisani, A., Ramella, M., Zucca, E., & Zamorani, G. 1998, MNRAS, 300, 589

Bardelli, S., Schinnerer, E., Smolic, V., et al. 2011, A&A, 511, A1

Bardelli, S., Zucca, E., Vettolani, G., et al. 1994, MNRAS, 267, 665

Barrena, R., Boschin, W., Girardi, M., & Spolaor, M. 2007, A&A, 469, 861

Barrena, R., Girardi, M., Boschin, W., & Dasí, M. 2009, A&A, 503, 357

Barrena, R., Ramella, M., Boschin, W., et al. 2005, A&A, 444, 685

Beers, T. C., Flynn, K., & Gebhardt, K. 1990, AJ, 100, 32

Beers, T. C., Forman, W., Huchra, J. P., Jones, C., & Gebhardt, K. 1991, AJ, 102, 1581

Beers, T. C., Gebhardt, K., Huchra, J. P., et al. 1992, ApJ, 400, 410

Beers, T. C., Geller, M. J., & Huchra, J. P. 1982, ApJ, 257, 23

Bekki, K., Owers, M. S., & Couch, W. J. 2010, ApJ, 718, L27

Bertin, E., & Arnouts, S. 1996, A&AS, 117, 393

Bird, C. M. 1994, AJ, 107, 1637

Bird, C. M., & Beers, T. C. 1993, AJ, 105, 1596

Biviano, A., Katgert, P., Thomas, T., & Adami, C. 2002, A&A, 387, 8

Biviano, A., Murante, G., Borgani, S., Diaferio, A., Dolag, K., & Girardi, M. 2006, A&A, 456, 23

Bonafede, A., Feretti, L., Giovannini, G., et al. 2009, A&A, 503, 707

Boschin, W., Girardi, M., Spolaor, M., & Barrena, R. 2006, A&A, 449, 461

Boschin, W., Barrena, R., & Girardi, M. 2010, A&A, 521, A78

Brunetti, G., Cassano, R., Dolag, K., & Setti, G. 2009, A&A, 507, 661

Bullock, J. S., Kolatt, T. S., Sigad, Y., et al. 2001, MNRAS, 321, 559

Buote, D. A. 2001, ApJ, 553, L15

Buote, D. A. 2002, in "Merging Processes in Galaxy Clusters", eds. L. Feretti, I. M. Gioia, & G. Giovannini (The Netherlands, Kluwer Ac. Pub.): Optical Analysis of Cluster Mergers

Buote, D. A., & Tsai, J. C. 1996, ApJ, 458, 27

Carlberg, R. G., Yee, H. K. C., & Ellingson, E. 1997, ApJ, 478, 462

Cappellari, M., & Copin, Y. 2003, MNRAS, 342, 345

Cassano, R., & Brunetti, G. 2005, MNRAS, 357, 1313

Cassano, R., Brunetti, G., Röttgering, H. J. A., & Brüggen, M. 2010a, A&A, 509, A68

Cassano, R., Brunetti, G., & Setti, G. 2006, MNRAS, 369, 1577

Cassano, R., Brunetti, G., Setti, G., Govoni, F., & Dolag, K. 2007, MNRAS, 378, 1565

Cassano, R., Ettori, S., Giacintucci, S., et al. 2010b, ApJ, 721, 82

Cavagnolo, K. W., Donahue, M., Voit, G. M., & Sun, M. 2009, ApJS, 182, 12

Churazov, E., Tremaine, S., Forman, W., et al. 2010, MNRAS, 404, 1165

Crawford, C. S., Edge, A. C., Fabian, A. C., et al. 1995, MNRAS, 274, 75

Danese, L., De Zotti, C., & di Tullio, G. 1980, A&A, 82, 322

den Hartog, R., & Katgert, P. 1996, MNRAS, 279, 349

Diehl, S., & Statler, T. S. 2006, MNRAS, 368,497

Dolag, K., Bartelmann, M., Perrotta, F., et al. 2004, A&A, 416, 853

Dressler, A., & Shectman, S. A. 1988, AJ, 95, 985

Durret, F., Laganá, T. F., & Bertin, E. 2010, A&A, 517, A94

Ebeling, H., Voges, W., Böhringer, H., et al. 1996, MNRAS, 281, 799

Ellingson, E., & Yee, H. K. C. 1994, ApJS, 92, 33

Ensslin, T. A., Biermann, P. L., Klein, U., & Kohle, S. 1998, A&A, 332, 395

Ensslin, T. A., & Gopal-Krishna 2001, A&A, 366, 26

Ensslin, T. A., Pfrommer, C., Miniati, F., & Subramanian, K. 2011, A&A, 527, A99

Ettori, S., Gastaldello, F., Leccardi, A., et al. 2010, A&A, 524, A68

Fadda, D., Girardi, M., Giuricin, G., Mardirossian, F., & Mezzetti, M. 1996, ApJ, 473, 670

Fasano, G., & Franceschini, A. 1987, MNRAS, 225, 155

Feretti, L. 1999, MPE Report No. 271

Feretti, L. 2002a, The Universe at Low Radio Frequencies, Proceedings of IAU Symposium 199, held 30 Nov – 4 Dec 1999, Pune, India. Edited by A. Pramesh Rao, G. Swarup, and Gopal-Krishna, 2002., p.133

Feretti, L. 2005, X-Ray and Radio Connections (eds. L. O. Sjouwerman and K. K. Dyer). Published electronically by NRAO, http://www.aoc.nrao.edu/events/xraydio. Held 3–6 February 2004 in Santa Fe, New Mexico, USA

Feretti, L., Gioia I. M., and Giovannini G. eds., 2002b, Astrophysics and Space Science Library, vol. 272, "Merging Processes in Galaxy Clusters", Kluwer Academic Publisher, The Netherlands

Ferrari, C., Govoni, F., Schindler, S., Bykov, A. M., & Rephaeli, Y. 2008, Space Sci. Rev., 134, 93

Ferrari, C., Maurogordato, S., Cappi, A., & Benoist C. 2003, A&A, 399, 813

Gal, R. R., de Carvalho, R. R., Lopes, P. A. A., et al. 2003, AJ, 125, 2064

Gastaldello, F., Buote, D. A., Humphrey, P. J., et al. 2007, ApJ, 662, 923

Geller, M. J., & Beers, T. C. 1982, PASP, 94, 421

Giovannini, G., Bonafede, A., Feretti, L., et al. 2009, A&A, 507, 1257

Giovannini, G., & Feretti, L. 2002, in "Merging Processes in Galaxy Clusters", eds. L. Feretti, I. M. Gioia, & G. Giovannini (The Netherlands, Kluwer Ac. Pub.): Diffuse Radio Sources and Cluster Mergers

Giovannini, G., Tordi, M., & Feretti, L. 1999, New Astronomy, 4, 141

Girardi, M., Barrena, R., & Boschin, W. 2007, Contribution to "Tracing Cosmic Evolution with Clusters of Galaxies: Six Years Later" conference – http://www.si.inaf.it/sesto2007/contributions/Girardi.pdf

Girardi, M., Barrena, R., Boschin, W., & Ellingson, E. 2008, A&A, 491, 379

Girardi, M., & Biviano, A. 2002, in "Merging Processes in Galaxy Clusters", eds. L. Feretti, I. M. Gioia, & G. Giovannini (The Netherlands, Kluwer Ac. Pub.): Optical Analysis of Cluster Mergers

Girardi, M., Borgani, S., Giuricin, G., Mardirossian, F., & Mezzetti, F. 2000, ApJ, 530, 62

Girardi, M., Escalera, E., Fadda, D., et al. 1997, ApJ, 482, 11

Girardi, M., Fadda, D., Giuricin, G. et al. 1996, ApJ, 457, 61

Girardi, M., Giuricin, G., Mardirossian, F., Mezzetti, M., & Boschin, W. 1998, ApJ, 505, 74

Girardi, M., & Mezzetti, M. 2001, ApJ, 548, 79

Goto, T., Sekiguchi, M., Nichol, R. C., et al. 2002, AJ, 123, 1807

Govoni, F., Ensslin, T. A., Feretti, L., & Giovannini, G. 2001a, A&A, 369, 441

Govoni, F., Feretti, L., Giovannini, G., et al. 2001b, A&A, 376, 803

Grevesse, N., & Sauval, A. J. 1998, Space Sci. Rev., 85, 161

Gullixson, C. A. 1992, in "Astronomical CCD Observing and Reduction techniques" (ed. S. B. Howell), ASP Conf. Ser., 23, 130

Henry, J. P., Briel, U. G., & Nulsen, P. E. J. 1993, A&A, 271, 413

Hoeft, M., Brüggen, M., & Yepes, G. 2004, MNRAS, 347, 389

Kalberla, P. M. W., Burton, W. B., Hartmann, D., et al. 2005, A&A, 440, 775 (LAB Map)

Kempner, J. C., Blanton, E. L., Clarke, T. E. et al. 2004, Proceedings of the conference "The Riddle of Cooling Flows in Galaxies and Clusters of Galaxies", eds. T. H. Reiprich, J. C. Kempner, & N. Soker, preprint arXiv: astro-ph/0310263

Kennicutt, R. C. 1992, ApJS, 79, 225

Keshet, U. 2011, MNRAS, submitted (preprint arXiv:1011.0729)

Kuntz, K. D. & Snowden, S. L. 2008, A&A, 478, 575

Landolt, A. U. 1992, AJ, 104, 340

Leccardi, A., & Molendi, S. 2008, A&A, 486, 359

Leccardi, A., Rossetti, M., & Molendi, S. 2010, A&A, 510, 82

Ledlow, M. J., & Owen, F. N. 1996, 112, 9

Loeb, A., & Mao, S. 1994, ApJ, 435, L109

Lu, T., Gilbank, D. G., Balogh, M. L., & Bognat, A. 2009, MNRAS, 399, 1858

Lubin, L. M., Brunner, R., Metzger, M. R., Postman, M., Oke, J. B. 2000, ApJ, 531, 5

Macario, G., Markevitch, M., Giacintucci, S., et al. 2011, ApJ, 728, 82

Malumuth, E. M., Kriss, G. A., Dixon, W. Van Dyke, Ferguson, H. C., & Ritchie, C. 1992, AJ, 104, 495

Markevitch, M. 2010, proceedings at "12th Marcel Grossman Meeting", Paris, July 2009 (updated with 2010 results), preprint arXiv:1010.3660

Markevitch, M., Gonzalez, A. H., David, L., et al. 2002, ApJ, 567, L27

Mohr, J. J., Fabricant, D. G., & Geller, M. J. 1993, ApJ, 413, 492

Mushotzky, R. F., & Scharf, C. A. 1997, ApJ, 482, L13

Navarro, J. F., Frenk, C. S., & White, S. D. M. 1997, ApJ, 490, 493

Nonino, M., Dickinson, M., Rosati, P., et al. 2009, ApJS, 183, 244

O'Hara, T. B., Mohr, J. J., Bialek, J. J., & Evrard, A. E. 2006, ApJ, 639, 64

Owen, F., Morrison, G., & Voges, W. 1999, proceedings of the workshop "Diffuse Thermal and Relativistic Plasma in Galaxy Clusters", eds. H. Böhringer, L. Feretti, & P. Schuecker, MPE Report 271, pp. 9–11

Owers, M. S., Randall, S. W., Nulsen, P. E., et al. 2011, ApJ, 728, 27

Pinkney, J., Roettiger, K., Burns, J.O., & Bird, C.M. 1996, ApJS, 104, 1

Pisani, A. 1993, MNRAS, 265, 706

Pisani, A. 1996, MNRAS, 278, 697

Poole, G. B., Fardal, M. A., Babul, A., et al. 2006, MNRAS, 373, 881

Popesso, P., Biviano, A., Böehringer, H., Romaniello, M., & Voges, W. 2005, A&A, 433, 431

Press, W. H., Teukolsky, S. A., Vetterling, W. T., & Flannery, B. P. 1992, in Numerical Recipes (Second Edition), (Cambridge University Press)

Quintana, H., Carrasco, E. R., & Reisenegger, A. 2000, AJ, 120, 511

Ramella, M., Biviano, A., Pisani, A., et al. 2007, A&A, 470, 39

Ramella, M., Boschin, W., Fadda, D., & Nonino, M. 2001, A&A, 368, 776

Rizza, E., Morrison, G. E., Owen, F. N., et al. 2003, AJ, 126, 119

Roettiger, K., Burns, J. O., & Loken, C. 1996, ApJ, 473, 651

Roettiger, K., Burns, J. O., & Stone, J. M. 1999, ApJ, 518, 603

Roettiger, K., Loken, C., & Burns, J. O. 1997, ApJS, 109, 307

Rossetti, M., Ghizzardi, S., Molendi, S., Finoguenov, A., 2007, A&A, 463, 839

Rossetti, M., Eckert, D., Cavalleri, B. M., et al. 2011 preprint arXiv:1106.4563

Rossetti, M., & Molendi, S., 2010, A&A, 510, 83

Sanderson, A. J. R., Ponman, T. J., & O'Sullivan, E. 2006, MNRAS, 372, 1496

Santos, J. S., Rosati, P., Tozzi, P., et al. 2008, A&A, 483, 35

Sarazin, C. L. 2002, in "Merging Processes in Galaxy Clusters", eds. L. Feretti, I. M. Gioia, & G. Giovannini (The Netherlands, Kluwer Ac. Pub.): The Physics of Cluster Mergers

Sarazin, C. L. 2004, *Journal of the Korean Astronomical Society*, 37, 433

Saxton, R. D. & Siddiqui, H. 2002, XMM-SOC-PS-TN-43

Schlegel, D. J., Finkbeiner, D. P., & Davis, M. 1998, ApJ, 500, 525

Schuecker, P., Böhringer, H., Reiprich, T. H., & Feretti, L. 2001, A&A, 378, 408

Serna, A., & Gerbal, D. 1996, A&A, 309, 65

Smith, J. A., Tucker, D. L., Kent, S., et al. 2002, AJ, 123, 2121

Struble, M. F. & Rood, H. J. 1987, ApJS, 63, 555

Thompson, L. A. 1982, in IAU Symposium 104, Early Evolution of the Universe and the Present Structure, eds. G. O. Abell and G. Chincarini (Dordrecht: Reidel)

Tonry, J., & Davis, M. 1979, ApJ, 84, 1511

Tribble, P. C. 1993, MNRAS, 261, 57

Venturi, T., Giacintucci, S., Macario, G., et al. 2008, A&A, 484, 327

Wainer, H., & Schacht, S. 1978, Psychometrika, 43, 203

West, M. J., & Bothun , G. D. 1990, ApJ, 350, 36
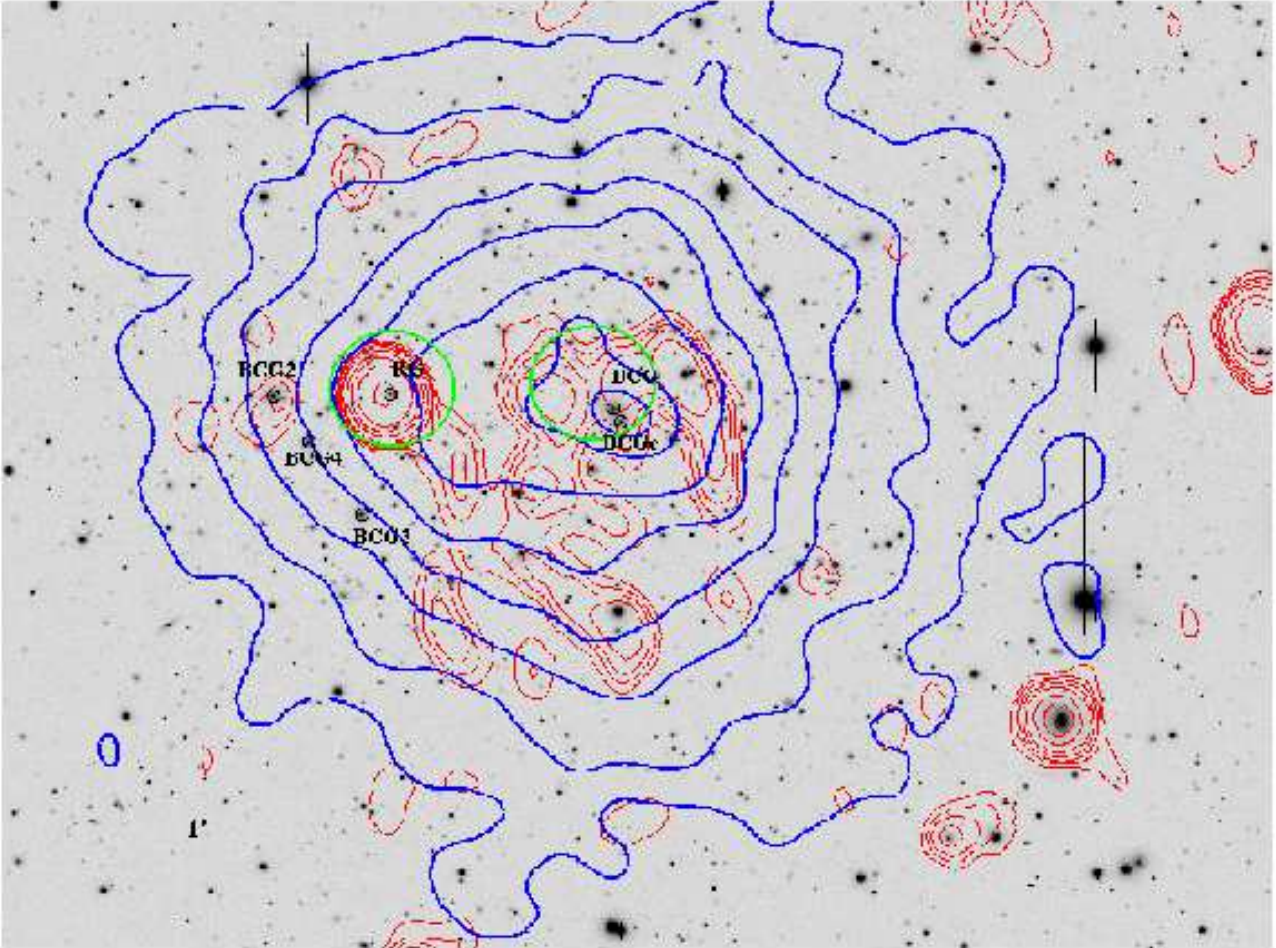
Fig. 1. Subaru V-band image of the cluster A2254 (North at the top and East to the left) with, superimposed, the contour levels of the XMM archival image (thick/blue contours; photons in the energy range 0.5–2 keV) and the contour levels of a VLA radio image at 1.4 GHz (thin/red contours, see Govoni et al. 2001b). Labels indicate galaxies cited in the text. The two (green) circles indicate the positions of the E- and W-peaks in the galaxy distribution from the 2D-DEDICA analysis (Subaru sample, with $i' \leq 20.5$ mag, see Tab. 2).
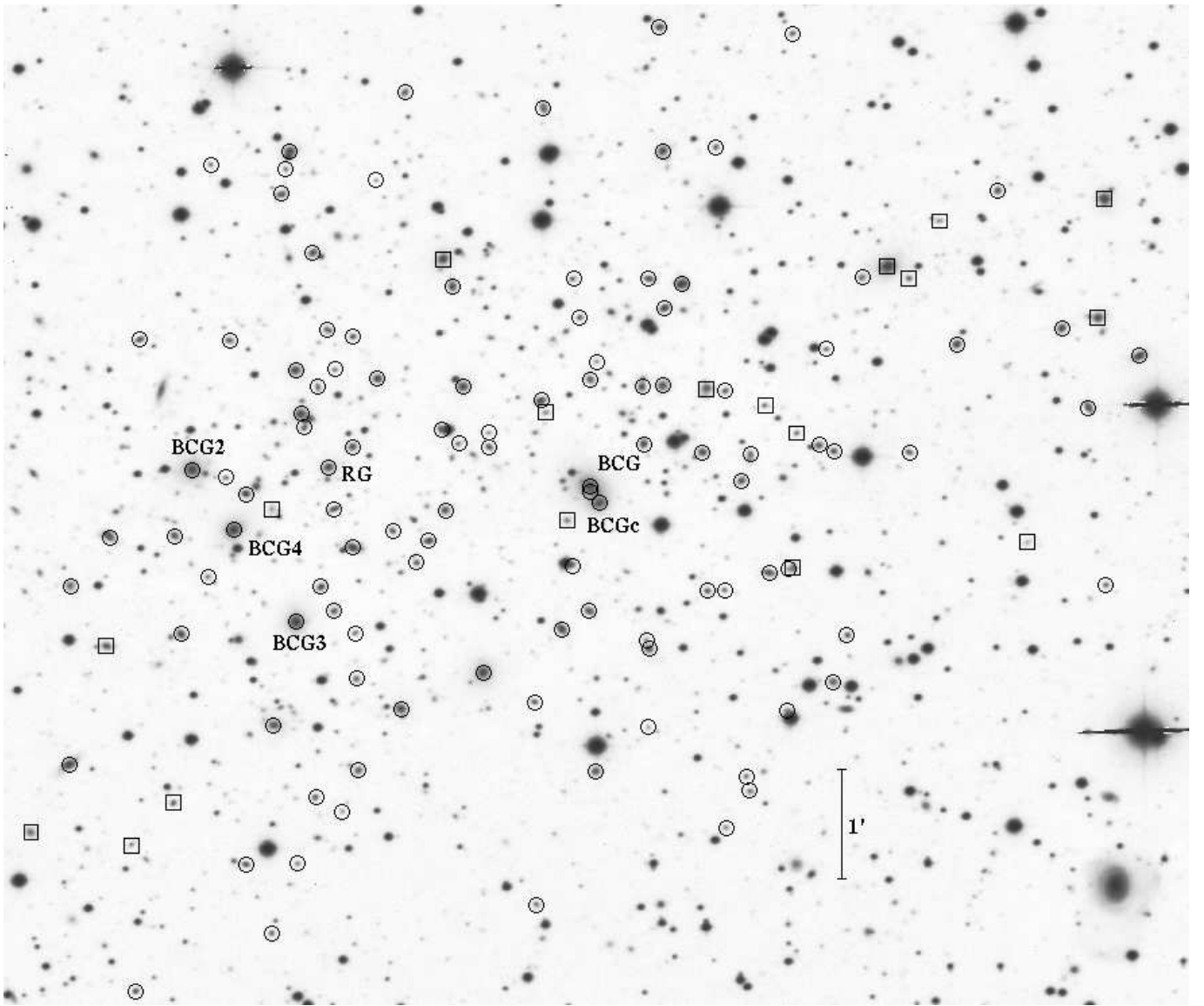
Fig. 2. INT r'-band image of the cluster A2254 (North at the top and East to the left). Circles and squares indicate cluster members and non-members, respectively (see Table 1). Labels indicate cluster galaxies cited in the text.
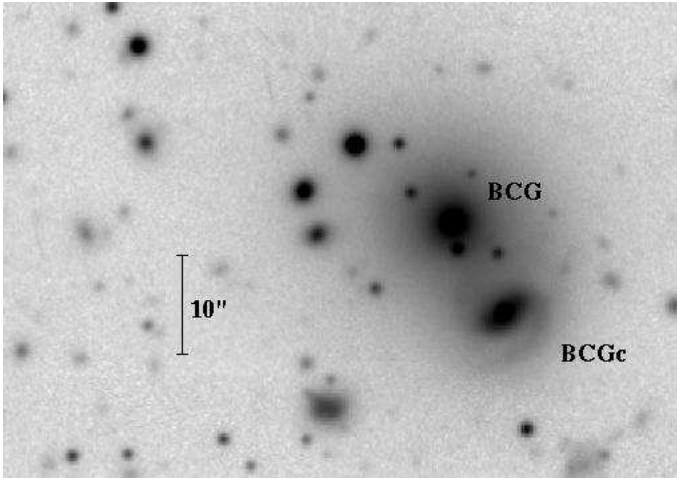
Fig. 3. Subaru *i'*-band image of the very central cluster region. It highlights the BCG and its bright spiral companion BCGc (North at the top and East to the left).
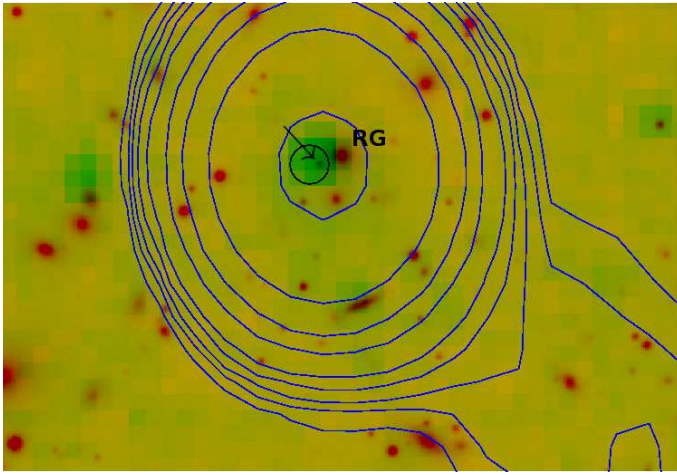
Fig. 4. Multiwavelength picture of the region around RG galaxy. The MIPS-Spitzer image (green color) is superimposed to the Subaru *i'*-band image. The arrow indicates the faint extended object close to RG. The black circle indicate the position of the XMM point source. Contour levels of the radio image are shown in blue (Govoni et al. 2001b). North at the top and East to the left.